Traffic 2009; **10:** 691–712
Blackwell Munksgaard

doi: 10.1111/j.1600-0854.2009.00902.x

Dynamic Partitioning of a Glycosyl-Phosphatidylinositol-Anchored Protein in Glycosphingolipid-Rich Microdomains Imaged by Single-Quantum Dot Tracking

Fabien Pinaud[1,3,*], Xavier Michalet[1,*], Gopal Iyer[1], Emmanuel Margeat[1,4], Hsiao-Ping Moore[2,5] and Shimon Weiss[1*]

[1]Department of Chemistry and Biochemistry, University of California at Los Angeles, Los Angeles, CA, USA
[2]Department of Molecular and Cell Biology, University of California at Berkeley, Berkeley, CA, USA
[3]Current address: Ecole Normale Supérieure Département de Biologie, 46 rue d' Ulm, 75005-Paris, France
[4]Current address: Centre de Biochimie Structurale, 29 Rue de Navacelles 34090, Montpellier, France
[5]Current address: Lawrence Technological University, 21000 West Ten Mile Road Southfield, MI 48075, USA
**Corresponding authors: Fabien Pinaud, fabien.pinaud@lkb.ens.fr; Xavier Michalet, michalet@chem.ucla.edu and Shimon Weiss, sweiss@chem.ucla.edu*

Recent experimental developments have led to a revision of the classical fluid mosaic model proposed by Singer and Nicholson more than 35 years ago. In particular, it is now well established that lipids and proteins diffuse heterogeneously in cell plasma membranes. Their complex motion patterns reflect the dynamic structure and composition of the membrane itself, as well as the presence of the underlying cytoskeleton scaffold and that of the extracellular matrix. How the structural organization of plasma membranes influences the diffusion of individual proteins remains a challenging, yet central, question for cell signaling and its regulation. Here we have developed a raft-associated glycosyl-phosphatidyl-inositol-anchored avidin test probe (Av-GPI), whose diffusion patterns indirectly report on the structure and dynamics of putative raft microdomains in the membrane of HeLa cells. Labeling with quantum dots (qdots) allowed high-resolution and long-term tracking of individual Av-GPI and the classification of their various diffusive behaviors. Using dual-color total internal reflection fluorescence (TIRF) microscopy, we studied the correlation between the diffusion of individual Av-GPI and the location of glycosphingolipid GM1-rich microdomains and caveolae. We show that Av-GPI exhibit a fast and a slow diffusion regime in different membrane regions, and that slowing down of their diffusion is correlated with entry in GM1-rich microdomains located in close proximity to, but distinct, from caveolae. We further show that Av-GPI dynamically partition in and out of these microdomains in a cholesterol-dependent manner. Our results provide direct evidence that cholesterol-/sphingolipid-rich microdomains can compartmentalize the diffusion of GPI-anchored proteins in living cells and that the dynamic partitioning raft model appropriately describes the diffusive behavior of some raft-associated proteins across the plasma membrane.

Key words: caveolae, cholera toxin B, cholesterol, fluorescence imaging, GM1 lipids, lipid rafts, live cell, membrane diffusion, particle tracking, single molecule microscopy

Received 21 May 2008, revised and accepted for publication 18 February 2009, uncorrected manuscript published online 27 March 2009, published online 17 April 2009

Over the years, the plasma membrane 'fluid mosaic' model proposed by Singer and Nicholson in their 1972 landmark review (1) has been significantly refined. Current models incorporate the notion that membranes are crowded environments (2) having a complex topology, and that they interact strongly with the cytoskeleton and contain microdomains of different sizes and lipid/protein composition (3–6). Several types of plasma membrane microdomains have been proposed: (i) domains delineated by transmembrane proteins attached to the underlying actin cytoskeletal network (7,8); (ii) domains formed by specific protein–protein interactions (9) or (iii) domains formed by the preferential association of certain lipids and proteins into cholesterol- and glycosphingolipid (GSL)-rich liquid ordered (L_o) phases, named lipid rafts (10,11). These various domains are thought to play a role in regulating specific molecular interactions by partitioning the plasma membrane and allowing the rapid assembly or disassembly of specific multiprotein/lipid complexes involved in cellular signaling (12).

Particular attention has been given to lipid rafts because they appear implicated in signal transduction, signal amplification and protein sorting (13,14). From a number of experimental approaches, it has been extrapolated that raft domains are generally enriched in cholesterol, in glycosphingolipids and in specific sets of proteins, notably in glycosyl-phosphatidylinositol-anchored proteins (GPI-AP), whose saturated fatty acyl anchor favor their packing with cholesterol and association with the L_o lipid phase (15,16). By studying the distribution of cholesterol, glycosphingolipids (such as GM1) or GPI-AP, 'raft-like' lipid phases have been observed in model membranes (17–20), and inferred from the isolation of detergent-resistant membranes (DRM) in cells (21).

Recent studies have confirmed the existence of lipid domains with different fluidities in cell plasma membranes (22,23). Overall, a growing amount of evidence indicates that lipid rafts are probably small, heterogeneous and highly dynamic (5,24,25). However, despite a multitude of techniques developed over the past 20 years (26), a distinct picture of their structure and dynamics is lacking, and it is still unclear how such domains may affect the diffusion and the partitioning of membrane proteins in live cells. Part of the problem is that such small and elusive structures require the use of high-temporal and spatial resolution observation techniques capable of correlating the location of different molecular components. Single-molecule spectroscopy and microscopy techniques are in principle well suited for this purpose as they give access to static and dynamic molecular heterogeneities (27). Among these techniques, image correlation spectroscopy (ICS) and fluorescence correlation spectroscopy (FCS) have been employed to study the diffusion and clustering of integrins (28) and to identify lipid- and actin-dependent microdomains in live cells (29,30). Hetero- and homoFRET, as well as fluorescence polarization anisotropy, have been used to study the organization of membrane components at the nanometer scale (31). Tracking techniques, such as single-dye tracking (SDT) (32), single-particle tracking (SPT) (33–35) and, more recently, photothermal interference contrast imaging of gold nanoparticles (36), have also permitted the detection of membrane compartments and confinement zones of 30–700 nm for a variety of raft and non-raft lipids and proteins. Unfortunately, standard single-molecule fluorescence methods are often limited by rapid probe photobleaching, which reduces the duration of measurements and limits the observation of complex dynamics. On the other hand, non-fluorescent particle tracking, which does not suffer from this drawback, is not easily amenable to signal multiplexing, preventing the correlation of multiple parameters.

Quantum dots (Qdots) overcome most of these limitations. They are bright and extremely photostable fluorescent nanoparticles, which, once solubilized and functionalized, make good probes for single-molecule imaging and tracking in live cells (37). Qdots have previously been used for high-resolution membrane tracking of single proteins such as glycine receptors (38), AMPA and NMDA receptors (39), integrins (40) and CFTR channel proteins (41,42) among a growing list of many others.

Here, we used biotinylated peptide-coated qdots to track single GPI-anchored avidin test probes expressed in HeLa cells. Using dual-color total internal reflection fluorescence (TIRF) imaging and single-qdot tracking (SQT), we quantified their lateral diffusion and studied their interactions with glycosphingolipid GM1-rich microdomains of the plasma membrane and with caveolae. Our study reveals that GPI-anchored avidin dynamically partition in and out of GM1-rich microdomains, which are in close proximity to, but distinct, from caveolae. This partitioning is characterized by changes in diffusion coefficients and is cholesterol-dependent. Overall, these observations provide direct evidence that membrane microdomains having the accepted composition of lipid rafts can induce molecular compartmentalization in the cell plasma membrane, consistent with their putative function as protein sorting and signaling platforms.

Results

GPI-anchored avidin tetramers are found in DRM and associate with GM 1-rich lipid domains in HeLa cells

To investigate the structure and dynamics of membrane microdomains by single-molecule techniques, we designed a minimal GPI-anchored test probe having no biological functions, no specific interactions with other membrane components and a binding domain allowing its detection at extremely low concentration of fluorescent probes (<5 pM). This test probe consists of the full-length chicken avidin fused with the GPI-anchoring signal peptide of the human CD14 receptor (43) (Figure 1A). CD14 is a raft-associated GPI-anchored receptor for lipopolysaccharide normally expressed in monocytes (44–46), while avidin is absent from mammalian cells and has a very high affinity for biotin ($K_D \sim 10^{-15}$ M (47)). The post-translational modification of this avidin-fusion protein with a GPI anchor (Av-GPI) resulted in its anchoring to the plasma membrane. When stably expressed in HeLa cells, at expression levels comparable to those of a standard housekeeping gene [glyceraldehyde 3-phosphate dehydrogenase (GAPDH), data not shown], Av-GPI was efficiently targeted to the outer membrane leaflet, where it was homogeneously distributed with no mislocalization or aggregation (Figure 1B). Analysis of its oligomeric state from cell membrane preparations and comparison to native chicken avidin indicated that Av-GPI exist essentially as stable tetramers in the plasma membrane and do not form higher-order oligomers as previously reported for a similar LDL receptor-avidin fusion protein (48) (Figure S2).

In cells, GPI-anchoring sorts CD14 receptors to DRM consistent with their association with lipid rafts as defined biochemically (21,45,46). We therefore examined whether the GPI-anchoring signal peptide of CD14 promoted a similar sorting of avidin tetramers. In DRM preparations, Av-GPI was found enriched in the buoyant/light fraction, while the endogenous transferrin receptor (TfR), used as a non-raft associated protein control, was localized in the denser, non-raft fraction (Figure 1C). As often observed for native GPI-AP, the association of Av-GPI with DRM was cholesterol-dependent (49). Inhibition of cholesterol synthesis with lovastatin led to a partial redistribution of Av-GPI into the non-raft fraction, but did not affect the distribution of TfR (Figure 1C; Table S1). This repartition was accompanied by a specific reduction in the recovery of Av-GPI.

The apparent association of Av-GPI with putative membrane rafts was further confirmed by co-clustering with

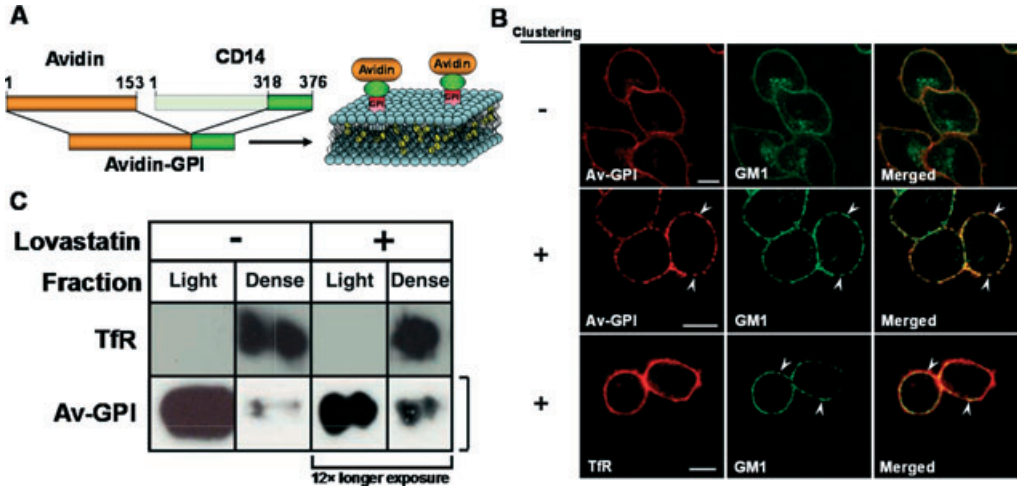

Figure 1: GPI-anchored avidin is targeted to the outer plasma membrane of HeLa cells and associates with lipid rafts as biochemically defined. A) Schematic representation of the avidin/CD14 fusion (Av-GPI) construct. The full-length chicken avidin (amino acids 1–153) was fused in frame with the GPI-anchor sequence of CD14 (amino acids 318–376) to target Av-GPI to the outer membrane of HeLa cells. B) Distribution of Av-GPI and GM1 in the membrane of HeLa cells with (+) or without (–) cross-linking with anti-avidin antibodies. Cross-linking induces the coclustering of Av-GPI and GM1 (see also data at http://fpinaud.bol.ucla.edu/index_files/Traffic.htm). Under the same conditions, endogenous transferrin receptors (TfR, non-raft proteins) remain evenly distributed (bottom row). Scale bars: 10 μm. C) Av-GPI are enriched in DRM. After cold detergent extraction and sucrose gradient separation, most Av-GPI (96%, Table S1) are found in the light/DRM-rich fraction, while the non-raft transferrin receptors (TfR, 97%) are in the dense fraction. Cholesterol depletion with lovastatin induces a partial repartitioning of Av-GPI into the dense fraction (36%) and a reduced recovery of Av-GPI (10% of untreated). Lovastatin has no effect on the total protein recovery, the recovery of TfR or their distribution.

glycosphingolipids GM1, which are often found to be associated with raft domains in cells (10,21,50). Upon cross-linking with anti-avidin antibodies, Av-GPI redistributed into patches (Figure 1 and additional data available at http://fpinaud.bol.ucla.edu/index_files/Traffic.htm). Staining with fluorescent cholera-toxin B subunit (CTxB), a high affinity marker of GM1 (51), revealed GM1 patching and co-clustering with Av-GPI. In contrast, cross-linking of Av-GPI did not induce the patching of TfR, which remained homogeneously distributed and showed no specific co-localization with GM1 patches (Figure 1B). Hence, Av-GPI and GM1 can occupy common membrane lipid domains, while TfR appear to reside in separate domains.

Thus, the avidin GPI-anchored test probe is properly expressed and sorted in HeLa cells. While native GPI-AP are generally monomeric, Av-GPI tetramers are representative of native raft-markers because they associate in a cholesterol-dependent manner with DRM and with glycosphingolipid GM1-rich domains of the outer plasma membrane.

Long-term single-molecule tracking of Av-GPI using qdots

We then studied the dynamic properties of Av-GPI in more detail by TIRF and SQT. We used biotin and polyethylene glycol (PEG)-modified CdSe/ZnS qdots previously developed for single-molecule imaging in live cells (37,43). These small qdots (diameter: 13.0 ± 1.1 nm) could readily target Av-GPI in the ventral membrane of HeLa cells (Figure 2).

The diffusion trajectories of Av-GPI were studied for up to 2 min, and high-resolution localization of individual Av-GPI was done frame by frame (100 ms/frame), by fitting the diffraction-limited spot image of each qdot with a Gaussian function (52,53) (Figure 2B). Each tracked qdot displayed a characteristic on/off blinking behavior (54), confirming that we were following individual Av-GPI (Video 1). The typical position accuracy for the localization of Av-GPI was ~30 nm. The diffusion of each qdot-labeled Av-GPI was quantified by analyzing the mean square displacement (MSD) curve (33) and the probability distribution of square displacements (PDSD) for different time lags (55). PDSD analysis was often preferred over MSD analysis because it allows the unbiased detection of multiple diffusion regimes within single trajectories and the quantitative characterization of each regime, as verified on Monte Carlo simulated trajectories (Figure S5).

Using PDSD analysis, we determined whether each Av-GPI experienced a single or multiple diffusion regimes. For each detected diffusion regime, we measured a diffusion coefficient and classified the regime into one of four categories (Figure 2D): (i) pure Brownian diffusion, (ii) restricted diffusion, for diffusions limited by corrals or impaired by obstacles, (iii) directed diffusion, for diffusion dominated by a velocity component, and (iv) no diffusion,

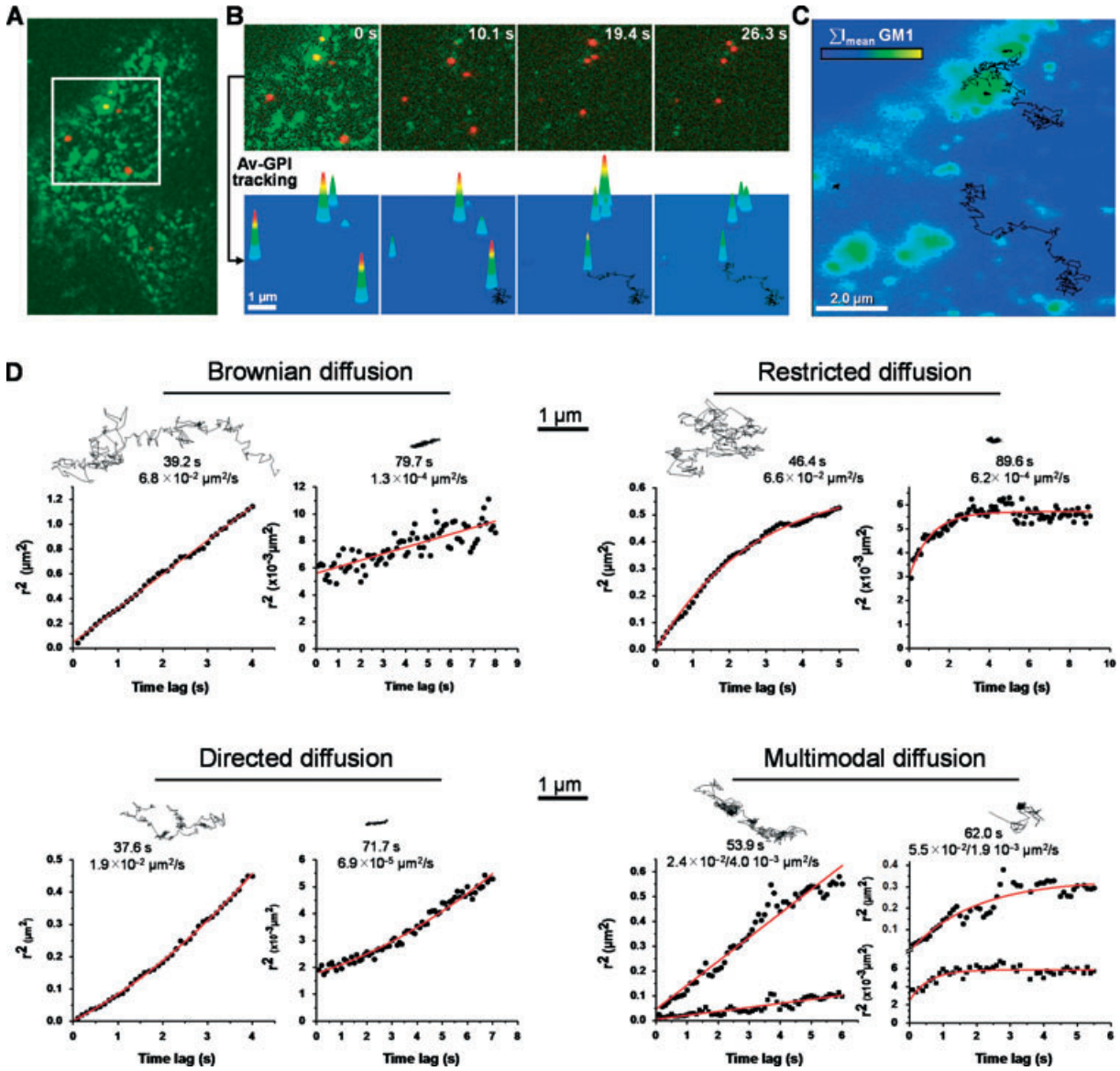

Figure 2: Single qdot tracking of Av-GPI by total internal reflection fluorescence (TIRF) microscopy, quantification and classification of diffusion modes. A) First frame from a dual-color TIRF movie of a HeLa cell. Av-GPI in the ventral plasma membrane are labeled with qdots (red) and GM1 are labeled with Alexa-488 CTxB (green). B) Selected frames from a region of interest [white square in (A)] in which diffusing Av-GPI are tracked. Diffusion trajectories are determined by the series of fitted positions, connected by a straight line. Notice that Alexa-488 CTxB bleaches fast compared to qdots and signal was nearly completely lost after 10 s (Video 3). To facilitate visualization, the qdot PSF size was intentionally expanded. Tracking was performed on raw images. C) Overlay of Av-GPI trajectories with the mean intensity projection image ($\sum I_{mean}$) for the Alexa-488 CTxB channel (see *Materials and Methods*). This approach allows colocalization studies of Av-GPI with fixed/slow diffusing GM1-rich domains despite the fast photobleaching of Alexa-488 CTxB (see data at http://fpinaud.bol.ucla.edu/index_files/Traffic.htm). D) Analysis by PDSD for various trajectories and classification into diffusion modes. PDSD analysis was done on the first 10% of time lags (t) (see *Materials and Methods*). The resulting $r_i^2(t)$ curves (black dots or squares) were fitted with either pure Brownian, restricted or directed diffusion models (red, Table S2). When an Av-GPI experienced changes in diffusion during tracking, multiple $r_i^2(t)$ curves were obtained and the mode of diffusion and the diffusion coefficient for each regime was determined. A representative sample of the various diffusion modes and diffusion coefficients of Av-GPI in HeLa cells are shown together with the corresponding trajectories and their duration. Notice that classification into various diffusion modes could not have been accurately performed by simple visual inspection of the trajectories.

for static Av-GPI with diffusion below a cut-off value $D_{min} = 4.8 \times 10^{-5}$ µm^2/s (see *Materials and Methods*). The diffusion coefficients from all regimes, evaluated for all qdot-labeled Av-GPI on multiple cells, were then reported in histograms having logarithmically spaced bins. The resulting histograms were fitted by one or two

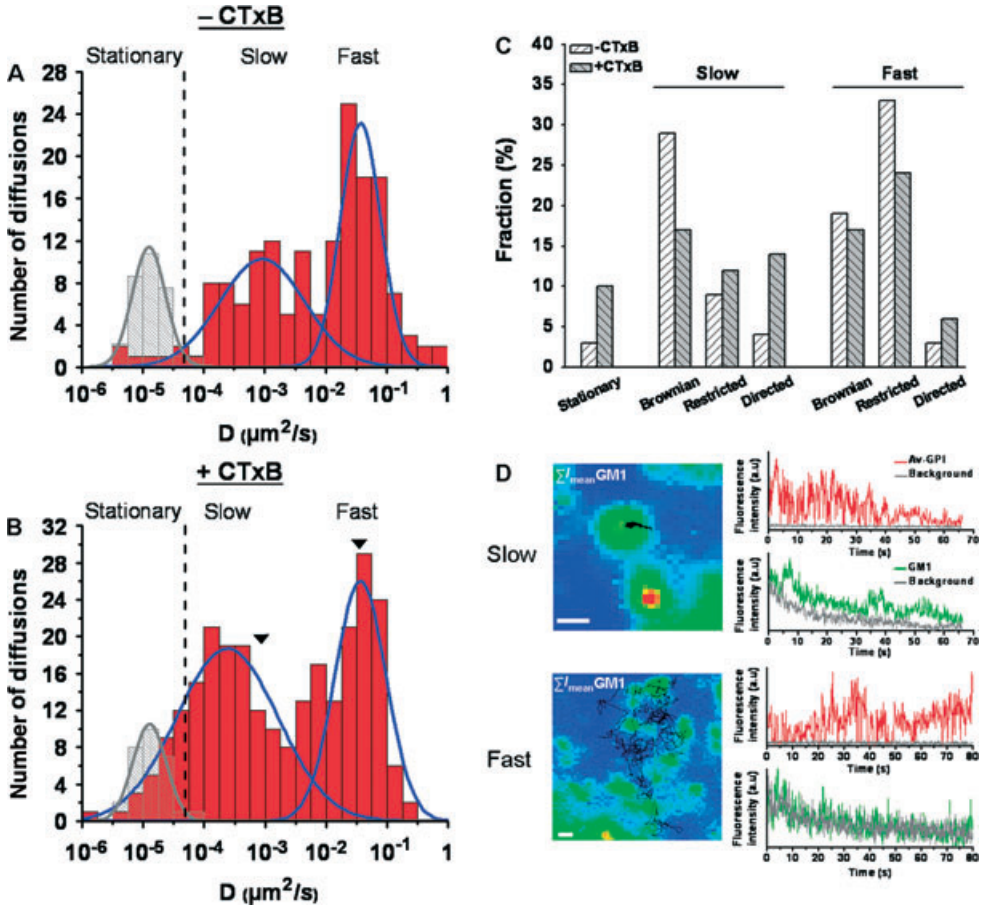

Figure 3: Bimodal diffusion of Av-GPI and interaction with GM1-rich microdomains. A) Distribution of Av-GPI diffusion coefficients (red *D*-histogram) in HeLa cells without GM1 staining (-CTxB). Two Av-GPI diffusion regimes (fast and slow) are recovered after PDSD analysis, with $\hat{D}_{fast} = 3.8 \times 10^{-2}$ μm²/ s (SE 3.2–4.5 × 10^{-2} μm²/ s, 55%) and $\hat{D}_{slow} = 9.1 \times 10^{-4}$ μm²/ s (SE 0.7–1.2 × 10^{-3} μm²/s, 42%). A *D*-histogram of qdots non-specifically bound to fibronectin (gray) is used to define immobile Av-GPI (3%). The fraction of Av-GPI switching between fast and slow diffusion is 22% (fraction determined using 1.3 × 10^{-2} μm²/ s as a cut-off diffusion value to separate slow and fast diffusion. This value encompasses 95% of the diffusion coefficients of the slow population). B) Distribution of Av-GPI diffusion coefficients in the presence of the GM1-marker Alexa 488 cholera toxin-B (+CTxB). CTxB specifically induces a fourfold reduction in diffusion for the slow Av-GPI subpopulation ($\hat{D}^{+CTxB}_{slow} = 2.4 \times 10^{-4}$ μm²/ s, SE 1.7–3.4 × 10^{-4} μm²/ s, 43%). Fast Av-GPI are unaffected ($\hat{D}^{+CTxB}_{fast} = 3.6 \times 10^{-2}$ μm²/ s, SE 2.9–4.6 × 10^{-2} μm²/ s, 47%). Arrowheads indicate the center of the distributions in the absence of CTxB in (A). C) Effect of CTxB on the diffusion modes for slow and fast Av-GPI subpopulations. The increase in directed diffusions and stationary molecules at the expense of pure Brownian diffusions indicates that CTxB restrict the mobility of slow Av-GPI. For the fast-diffusing subpopulation, CTxB only induces a moderate reduction of Av-GPI with restricted diffusions. D) Colocalization studies of Av-GPI with immobile/slow diffusing CTxB-labeled GM1 domains. Most of the slow Av-GPI (~70%) are found colocalized with GM1-rich microdomains, while fast Av-GPI avoid these domains. Colocalization observed from $\sum I_{mean}$ images are confirmed by correlating the fluorescence intensity time trace of qdot labeled Av-GPI (red) with the CTxB signal (green) along the diffusion trajectory. Because fluorescent signals varied from cell to cell, the background signal (gray) in close proximity to the trajectory is plotted for both red and green detection channels. Scale bars: 500 nm.

Gaussians, identifying as many populations of diffusion coefficients. In the following, we report the position of the peak (or mode) of these Gaussians (noted $\hat{D}$) as the characteristic diffusion coefficient of each population. Note that $\hat{D}$ is smaller than the mean value $\overline{D}$ of the distribution, yet $\hat{D}$ and $\overline{D}$ values differed at most by 40%, and our conclusions are unaffected by this choice.

For simplicity, we will henceforth talk about 'immobile', 'slow' and 'fast' diffusing Av-GPI, when referring to Av-GPI trajectories whose analysis yields immobile, slow and/or fast diffusion regimes, respectively.

Av-GPI exhibit multimodal diffusion

The diffusion coefficients of Av-GPI were distributed in two subpopulations of fast-diffusing ($\hat{D}^{SQT}_{fast} = 3.8 \times 10^{-2}$ μm²/ s, 55%) and slow-diffusing molecules ($\hat{D}^{SQT}_{slow} = 9.1 \times 10^{-4}$ μm²/ s, 42%) differing by about 40-fold in their modal diffusion coefficient (Figure 3A). We observed very few immobile Av-GPI ($D < D_{min}$, 3%). Within the duration

of our observation, most of the slow Av-GPI diffused with pure Brownian motion, while fast Av-GPI often experienced restricted diffusion (Figure 3C, −CTxB). Of all Av-GPI ($n = 118$), 66% had a single diffusion regime, while 31% exhibited two diffusion regimes and only 3% had three diffusion regimes. During tracking, we observed that 22% of all Av-GPI switched between fast and slow diffusion regimes (or vice versa). Other Av-GPI (12%) had two diffusion coefficients both belonging to the same distribution (either fast or slow), an indication that diffusion was more complex than a mere partitioning between fast and slow subpopulations.

The multimodal diffusion of Av-GPI and the values $\hat{D}_{\text{fast}}$ and $\hat{D}_{\text{slow}}$ were further confirmed by global analysis of the ensemble PDSDs (data can be viewed at http://fpinaud.bol.ucla.edu/index_files/Traffic.htm, $D_{\text{ens},1} = 3.8 \times 10^{-2}$ μm^2/s and $D_{\text{ens},2} = 6.4 \times 10^{-4}$ μm^2/ s). Thus, despite the wide diversity of diffusion coefficients demonstrated by Av-GPI, two predominant and very different diffusion regimes are observed in the membrane of HeLa cells.

To verify that this bimodal distribution of diffusion coefficients was not a consequence of transient or permanent clustering of Av-GPI by qdot-induced cross-linking, we performed tracking with quasi-monovalent biotinylated qdots (Figure S3). With these qdots, the same two subpopulations of fast- and slower-diffusing Av-GPI were detected, an indication that qdot valency has no effect on diffusion. We also confirmed the absence of cross-linking by SDT and FRAP of Av-GPI labeled with monovalent Alexa 488 biocytin. As described in more detail in Supporting Information, the analysis of single dye labeled-Av-GPI trajectories revealed a broad distribution of diffusion coefficients that included the same two prevalent diffusion regimes previously detected using qdots (Figure S4; Video 2). The diffusion coefficients of Av-GPI were about twice larger than those for qdots, suggesting that the larger size of qdots (∼13 nm compared to ∼2 nm for Alexa biocytin) induces a twofold decrease in diffusion coefficient. Two populations of diffusing Av-GPI were again detected by FRAP at room temperature (RT ∼ 27°C). Characteristic diffusion coefficients were as follows: $D_{\text{fast}}^{\text{FRAP}} = 6.5 \pm 1.9 \times 10^{-2}$ μm^2/ s and $D_{\text{slow}}^{\text{FRAP}} = 2.66 \pm 0.02 \times 10^{-3}$ μm^2/ s, comparable to those obtained by SDT and about twice those from SQT experiments (Figure S1). For both fast and slow Av-GPI subpopulations, the diffusion measured by SQT or FRAP at 37°C was three times faster than that at RT and well within the range expected for GPI-AP in HeLa cells (56) (data can be viewed at http://fpinaud.bol.ucla.edu/index_files/Traffic.htm and Figure S1). In addition, the respective fractions of each regimes were unchanged, an indication that working at RT did not significantly affect the membrane of HeLa cells.

SQT, SMT and FRAP indicate that, in the absence of probe-induced clustering, Av-GPI still experience two distinct diffusion regimes in the plasma membrane of HeLa cells, with a significant fraction (22%) switching from one diffusion regime to the other.

Interaction with stationary GM 1-rich microdomains induces the slow diffusion of Av-GPI

Because Av-GPI and GM1 can occupy common membrane lipid domains (Figure 1B), we tested whether these domains were responsible for the observed changes in diffusion regime, using dual-color TIRF imaging of qdot-labeled Av-GPI and Alexa 488-CTxB labeled GM1 (Figures 2 and 3; Video 3).

As before, SQT analysis yielded a bimodal distribution of diffusion coefficients. However, the addition of CTxB resulted in an approximately fourfold reduction of the diffusion coefficients for slow Av-GPI ($\hat{D}_{\text{slow}}^{+\text{CT}\times\text{B}} = 2.4 \times 10^{-4}$ μm^2/ s versus $\hat{D}_{\text{slow}}^{-\text{CT}\times\text{B}} = 9.1 \times 10^{-4}$ μm^2/ s), while fast Av-GPI were unaffected ($\hat{D}_{\text{fast}}^{+\text{CT}\times\text{B}} = 3.6 \times 10^{-2}$ μm^2/ s versus $\hat{D}_{\text{fast}}^{-\text{CT}\times\text{B}} = 3.8 \times 10^{-2}$ μm^2/ s) (Figure 3). CTxB also induced changes in diffusion of the slow population, consistent with a more restricted mobility. Namely, (i) the fraction of immobile molecules increased from 3 to 10%; (ii) the number of slow directed diffusions (possibly immobile Av-GPI located on slowly stretching or retracting patches of membrane) increased from 3 to 14% and (iii) the fraction of pure Brownian diffusion was reduced by half (Figure 3 C). Concomitantly, we found that the characteristic confinement radius of slow Av-GPI decreased from 152 nm (standard error or SE: 133–169 nm, $n = 13$) to 83 nm (SE: 69–100 nm, $n = 30$, data can be viewed at http://fpinaud.bol.ucla.edu/index_files/Traffic.htm).

In the CTxB detection channel, we detected the presence of mobile GM1, as well as membrane regions where GM1 diffused very slowly and appeared enriched (Video 3). In mean intensity projection images ($\sum I_{\text{mean}}$GM1), these stationary/slow diffusing GM1-rich regions formed a discontinuous phase comprising domains with sizes varying from a few microns to diffraction-limited spots (Figure 2C). When overlaid on CTxB intensity projection images, most of the slow diffusing Av-GPI (∼70%) colocalized with these stationary GM1-rich microdomains. Fast-diffusing Av-GPI were mainly restricted to the continuous unstained phase, sometimes appearing to traverse stained GM1 regions (Figure 3D, bottom panel). Among fast Av-GPI, those undergoing restricted diffusion appeared more confined after addition of CTxB, with a typical confinement radius decreasing from 640 nm (SE: 577–710 nm, $n = 57$) to 409 nm (SE: 356–470 nm, $n = 62$, data can be viewed at http://fpinaud.bol.ucla.edu/index_files/Traffic.htm). The addition of CTxB also reduced the number of Av-GPI switching from the fast to the slow regime or vice versa (11% versus 22% when CTxB was omitted). However, we were still able to observe few cases of Av-GPI entering and exiting stationary GM1-rich microdomains (Figure 4; Videos 4, 5 and 6). In these trajectories, entry in and exit from the microdomains correlated with

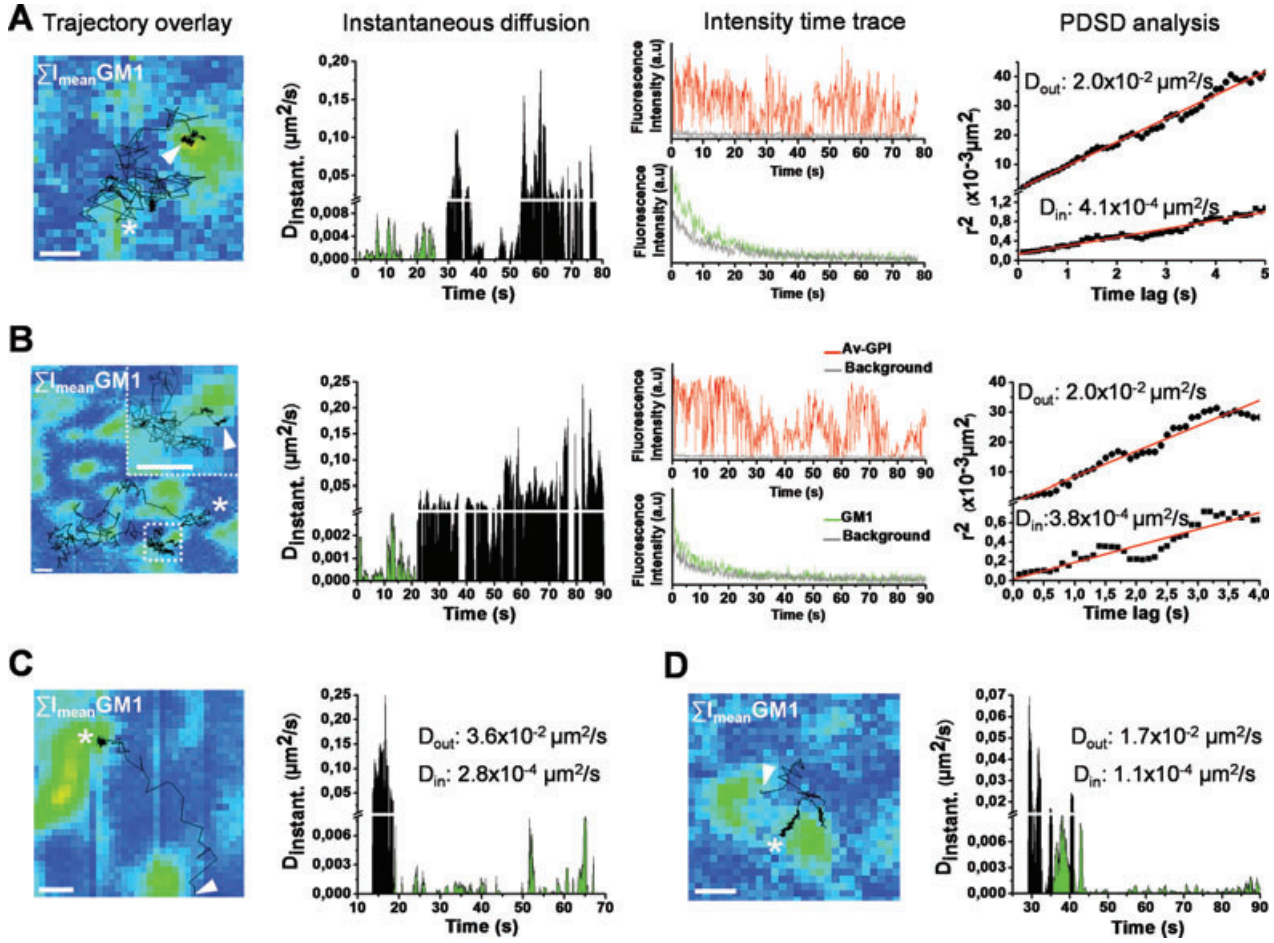

Figure 4: Dynamic partitioning of Av-GPI in and out of GM1-rich membrane microdomains. Example of Av-GPI exiting (A, B) or entering (C, D) cholera toxin B (CTxB) labeled GM1-rich microdomains (trajectory start: ▶/stop: ∗). For Av-GPI exiting GM1-rich domains (A, B), initial signal colocalization and subsequent absence of colocalization between qdot and CTxB is observed from trajectory overlay on $\sum I_{mean}$ images and from fluorescence intensity time traces. Domain exit correlates with an abrupt increase in the diffusion coefficient (instantaneous diffusions and PDSD analysis). Time periods where Av-GPI colocalize with GM1-rich domains are highlighted in green on instantaneous diffusion plots. The diffusion coefficients inside (D_{in}) and outside (D_{out}) GM1-rich domains are determined from subtrajectories MSD analysis and PDSD analysis (see *Material and Methods*). These diffusion values fall well within the distribution of diffusion coefficients for fast and slow Av-GPI determined in Figure 3B. Detecting the entry of Av-GPI in GM1-rich domains (C, D) relies mainly on trajectory overlay with $\sum I_{mean}$ images because labeled domains are usually bleached at the time of entry. Domain entry is associated with a clear reduction in diffusion coefficient. Notice that domains can be revisited (*D*). These trajectories are from untreated cells and cells treated with lovastatin. No difference in diffusive behaviors, interaction with GM1-rich domains or partitioning of Av-GPI was observed between both conditions. Scale bars: 500 nm.

marked changes in instantaneous diffusion coefficients, which clearly pertained to either the fast or the slow subpopulation. These rare events clearly demonstrated that interactions with stationary GM1-rich microdomains induced the slowing down of Av-GPI.

As seen from this analysis, GM1-rich microdomains in the membrane of HeLa cells are capable of compartmentalizing the diffusion of Av-GPI in two ways: (i) by inducing a reduction in the diffusion of Av-GPI by 1 to 2 orders of magnitude upon entry in microdomains and (ii) by acting as obstacles to fast Av-GPI diffusing outside these domains. Overall, these observations suggest that, in the plasma membrane, Av-GPI dynamically partition in two different lipid phases, which can compartmentalize their diffusion.

Av-GPI diffusion is slowed down in the proximity of caveolae

Next, we examined how membrane caveolae influenced the diffusion of Av-GPI. Caveolae are small (~ 50–100 nm diameters) plasma membrane invaginations having a lipid composition similar to that of lipid rafts and characterized by the presence of the scaffolding proteins caveolin-1 and 2 (25,57,58). GM1 has been shown to partially concentrate in caveolae in many cell types (59,60) and the addition of CTxB seems to further enhance its

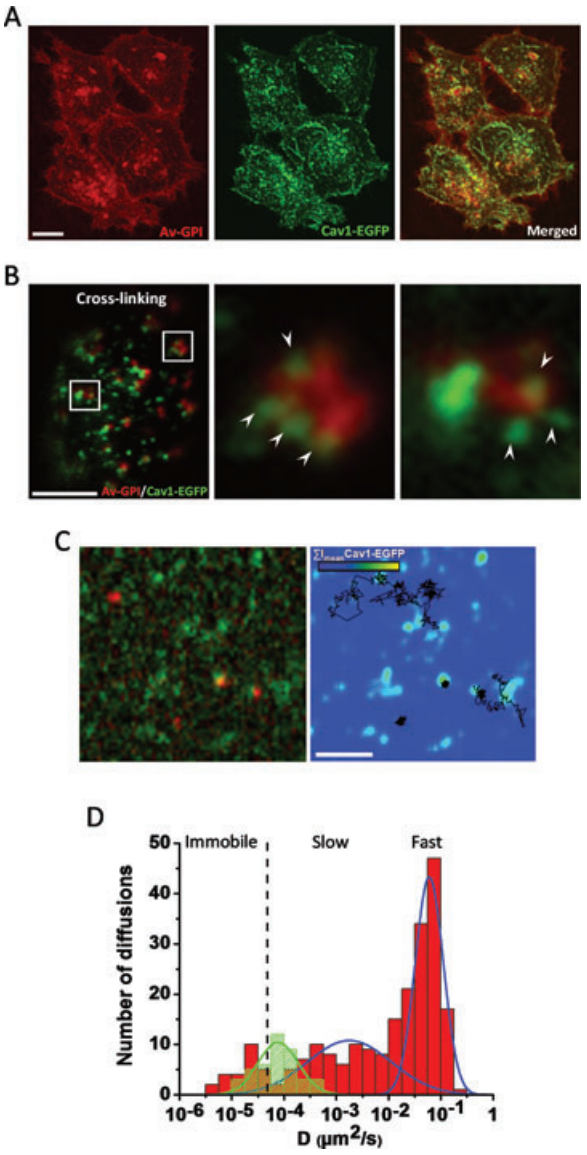

Figure 5: Imaging and tracking of Av-GPI and caveolae in HeLa cells. A) Confocal images of HeLa cells expressing Av-GPI and Cav1-EGFP. Scale bar: 10 μm. B) Cross-linking of Av-GPI with anti-avidin antibodies induces the formation of Av-GPI and GM1-rich patches located in caveolae-rich regions of the membrane. The magnified region of interest (white squares) shows that there is no extensive colocalization of these clusters with caveolar domains but that they are often contiguous (arrows). Scale bar: 5 μm. C) First frame from a dual-color TIRF movie of a HeLa cell coexpressing Av-GPI (red) and Cav1-EGFP (green, left panel). After tracking, Av-GPI trajectories are overlaid on the mean intensity image of Cav1-EGFP ($\sum I_{mean}$) to detect interactions with caveolae (right panel). Scale bar: 3 μm. D) Distribution of diffusion coefficients for Av-GPI (red) and caveolae (green). The two subpopulations of Av-GPI: fast ($\hat{D}_{fast}^{cav1-EGFP} = 6.0 \times 10^{-2}$ μm^2/s, SE 5.3–6.7 $\times 10^{-2}$ μm^2/s, 54%) and slow ($\hat{D}_{slow}^{cav1-EGFP} = 1.8 \times 10^{-3}$ μm^2/s, SE 0.9–3.5 $\times 10^{-3}$ μm^2/s, 36%) diffuse much faster than caveolae ($\hat{D}_{cav} = 7.7 \times 10^{-5}$ μm^2/s, SE 6.5–9.2 $\times 10^{-5}$ μm^2/s), an indication that Av-GPI are rarely immobilized within caveolae.

sequestering into these structures (61,62). The similar characteristics of caveolae and GM1-rich microdomains led us to investigate whether the changes of Av-GPI diffusion regimes were correlated with the location of these invaginations.

For this purpose, we developed a second HeLa cell line stably coexpressing both Av-GPI and caveolin-1-EGFP (Cav1-EGFP) (Figure 5A). This cell line exhibited a larger number of caveolae compared to our initial cell line with most caveolae containing Cav1-EGFP (data can be viewed at http://fpinaud.bol.ucla.edu/index_files/Traffic.htm). Despite a 10-fold lower membrane expression of Av-GPI (data can be viewed at http://fpinaud.bol.ucla.edu/index_files/Traffic.htm), good membrane staining was obtained with biotinylated probes (Figure 5A). Both Cav1-EGFP and Av-GPI were enriched in DRM and cross-linking induced the formation of membrane patches in which Av-GPI and GM1 were co-clustered (data not shown). These cross-linked Av-GPI/GM1 patches colocalized only poorly with caveolae (16 ± 6%), but were found in their proximity more frequently than expected by chance (Figure 5B and Supporting Information).

To study the spatial correlation between Av-GPI and caveolae in more detail, we used dual-color TIRF and SQT (Figure 5C; and Video 7). As previously reported (63,64), some caveolae diffused over short distances but most were essentially immobile ($\hat{D}_{cav} = 7.7 \times 10^{-5}$ μm^2/s, Figure 5D, green histogram) and easily identified in mean intensity images ($\sum I_{mean}$Cav1-EGFP). Qdot-labeled Av-GPI, on the other hand, were much more mobile and distributed as before into two diffusing subpopulations (Figure 5D; Video 7). The diffusion coefficients of fast ($\hat{D}_{fast}^{cav1\text{ - }EGFP} = 6.0 \times 10^{-2}$ μm^2/s, 54%) and slow Av-GPI ($\hat{D}_{slow}^{cav1\text{ - }EGFP} = 1.8 \times 10^{-3}$ μm^2/s, 36%) still differed by more than 1 order of magnitude, but were about twice as large as in cells expressing Av-GPI only. The characteristic radius of both fast (646 nm, SE: 562–741 nm, $n = 49$) and slow confined diffusions (131 nm, SE: 107–159 nm, $n = 29$) were unchanged.

When overlaid on $\sum I_{mean}$Cav1-EGFP images, fast Av-GPI were mainly found diffusing in between caveolae (Figure 6A), whereas slow ones were often located in regions containing many caveolae and diffused in domains adjacent to these structures (Figure 6B). For Av-GPI having two diffusion regimes (fast and slow), periods of slow diffusion frequently occurred in the proximity of caveolae (Figure 6 C; Figure S6). Only 15% ($n = 27$) of all the Av-GPI tracked exhibited confinement in caveolae as determined by colocalization (Figure 6D,E; Figure S6). Half of these colocalized Av-GPI (8%) had diffusion coefficients comparable to that of caveolae themselves, indicating possible immobilization in the cavities (Figure 6E; Figure S6). The other half (7%) had diffusion coefficients larger

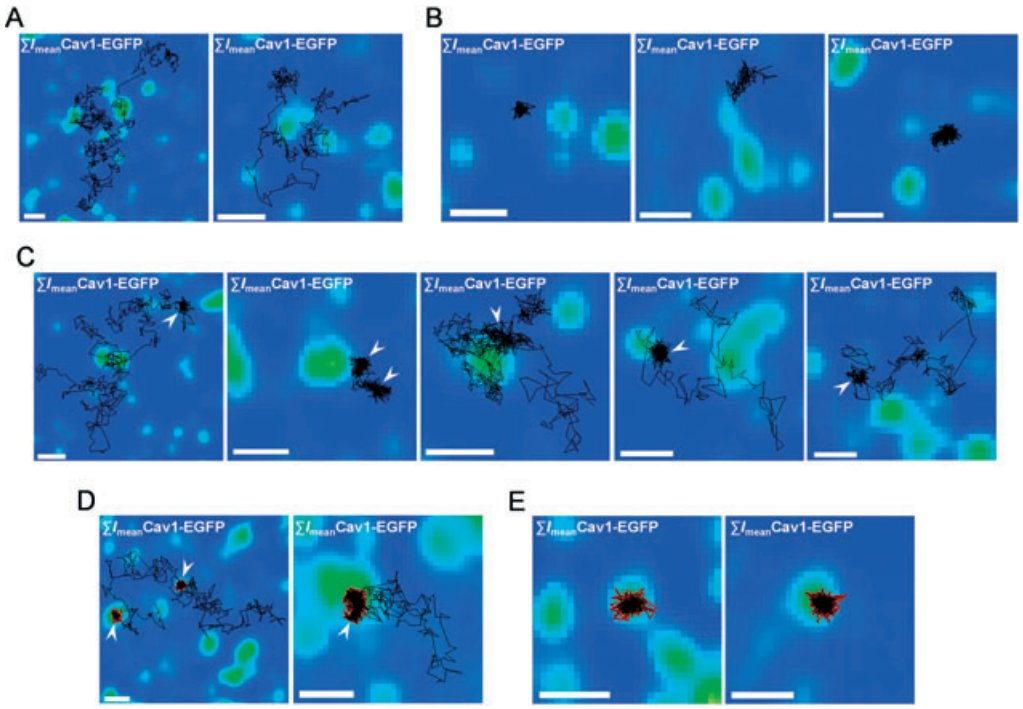

Figure 6: Tracking of Av-GPI reveals rare colocalization with caveolae but slower diffusion in their proximity. A) Fast Av-GPI diffuse mainly in caveolae-free part of the membrane. Colocalization with Cav1-EGFP labeled domains sometimes occurs but is not accompanied by apparent changes in diffusion. B) Slow diffusing Av-GPI are often found adjacent to caveolae. C) Examples of Av-GPI undergoing changes in diffusion during tracking. As in (B), intervals of slow diffusion (white arrows) often localize in close proximity to caveolae. D) On rare occasions, changes in diffusion upon direct interaction with caveolae are observed. Slow diffusion domains colocalizing with caveolae are highlighted in red and indicated by white arrows. E) Slow Av-GPI colocalized with caveolae have diffusion coefficients that may or may not be similar to that of the caveola itself, suggesting immobilization or simple confinement within the caveolar invagination (see also Figure S6). Scale bars (A–E): 1 μm.

than the associated caveolae and might simply have been confined (sometime transiently) within the invaginations (Figure 6D).

Despite a reduced membrane expression and the expression of Cav1-EGFP, Av-GPI maintained two main diffusion regimes. In addition, despite the high number of caveolae, entry and trapping into these cavities were too infrequent to account for the large number of diffusions pertaining to the slow regime. Clearly, slowing down of Av-GPI appears to be mainly induced by interaction with non-caveolar GM1-rich domains located in close proximity to caveolae, yet clearly distinct from caveolae themselves.

Acute cholesterol depletion slows down Av-GPI and restricts them to GM1-rich domains

We further studied how cholesterol, which promotes the formation of microdomains and controls lipid dynamic in membranes (30,65), influences the lateral diffusion of Av-GPI. Because the physical and functional properties of raft- and caveolae-associated molecules can be affected by a variety of cholesterol-depleting drugs (see (66) and references therein), we repeated our SQT experiments after treatment of HeLa cells with lovastatin or methyl-beta cyclodextrin (mβCD), two drugs that reduce cell cholesterol levels.

Lovastatin treatment (10 μM for 30 h) resulted in a ∼ 14% reduction in free cholesterol, but did not significantly decrease plasma membrane cholesterol levels compared to control cells (86 ± 22%, filipin staining, Figure S7). A partial disorganization of the cortical actin network was also observed (Figure S8) as previously reported for similar treatments of epithelial and endothelial cells (67,68). Av-GPI and GM1 appeared homogeneously distributed in the cell membrane, although CTxB staining after fixation and cell permeabilization revealed the presence of a small perinuclear pool of GM1 not present in untreated cells (Figure S8). The latter is consistent with the redistribution of sphingolipids to the Golgi apparatus upon cholesterol depletion (69). Despite these various effects, lovastatin treatment did not markedly influence the diffusion of Av-GPI or their interaction with GM1-rich domains (Video 8). When studied by SQT, both subpopulations of fast ($\hat{D}_{fast}^{+lova+CT\times B} = 2.8 \times 10^{-2}$ μm^2/s versus $\hat{D}_{fast}^{+CT\times B} = 3.6 \times 10^{-2}$ μm^2/ s) and slow ($\hat{D}_{slow}^{+lova+CT\times B} = 1.0 \times 10^{-4}$ μm^2/ s versus $\hat{D}_{slow}^{+CT\times B} = 2.4 \times 10^{-4}$ μm^2/ s) Av-GPI diffused with characteristics similar to untreated cells labeled with CTxB

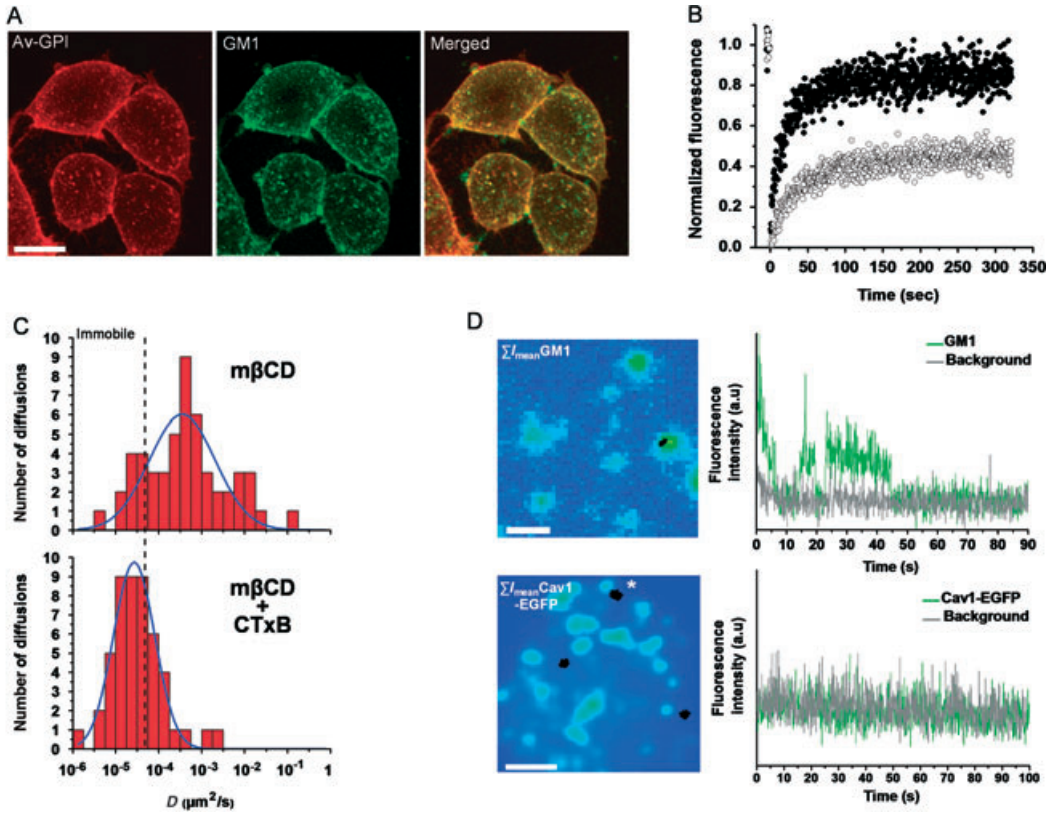

Figure 7: Acute cholesterol depletion by mβCD induces a slowing down of Av-GPI and an apparent redistribution in non-caveolar GM1-rich microdomains. A) Three-dimensional projection of live HeLa cells treated with mβCD for 1 h. Acute cholesterol depletion leads to the rounding up of cells, decreased Av-GPI surface density and redistribution of Av-GPI and GM1 into colocalizing punctuated domains in the membrane. Scale bar: 15 μm. B) FRAP of membrane Av-GPI directly after mβCD treatment (open circle) and after cholesterol replenishment (black circle). The diffusion of Av-GPI is reduced after treatment with mβCD but can be restored to pretreatment levels after reincubation into serum-supplemented media for 20 h. Both FRAP curves are averaged over three cells and acquired at 37°C. C) Distribution of Av-GPI diffusion coefficients after mβCD treatment (top panel) and mβCD treatment followed by imaging in the presence of cholera toxin B subunit (+CTxB, bottom panel). A single diffusing population of Av-GPI was recovered ($\hat{D}^{m\beta CD/-CTxB} = 3.5 \times 10^{-4}$ μm²/ s, SE 2.5–4.9 × 10^{-4} μm²/ s). The addition of CTxB induces an ~80−fold decrease in diffusion and nearly complete immobilization of Av-GPI ($\hat{D}^{m\beta CD/-CTxB} = 2.7 \times 10^{-5}$ μm²/ s, SE 2.2–3.3 × 10^{-5} μm²/ s). D) Correlation between Av-GPI trajectories and GM1-rich domains (top panel) or Cav1-EGFP domains (bottom panel) in mβCD-treated HeLa cells. About 50% of Av-GPI colocalized with slow/immobile CTxB-labeled GM1-rich microdomains. Fluorescent CTxB signal along the trajectory of Av-GPI indicates that Av-GPI interact directly with these domains. After mβCD-treatment Av-GPI diffused in domains adjacent to but distinct from caveolae, as verified by the absence of Cav1-EGFP fluorescent signal along the trajectory of the Av-GPI (marked by an asterisk). Scale bars: 1 μm (top) and 2 μm (bottom).

(Figure S9). The fractions of fast and slow diffusions were unchanged despite a broader distribution for fast Av-GPI.

mβCD (10 mM for 1 h) was a much more potent cholesterol-depletion agent and resulted in a ~60% reduction in free cholesterol and a dramatic decrease in plasma membrane cholesterol levels compared to control cells (17 ± 7%, filipin staining, Figure S7). Cells slightly rounded up after treatment (Figure 7A).The cortical actin network was affected to a lesser extent than with lovastatin with the appearance of microspikes and some actin-rich foci (Figure S8). However, depletion of GM1 from the plasma membrane and redistribution to perinuclear compartments were significantly higher than for the lovastatin treatment (Figure S8). A fourfold reduction in Av-GPI surface density was also detected by FACS (data not shown). Confocal imaging of live mβCD-treated HeLa cells confirmed the low membrane levels of Av-GPI and GM1, but also revealed punctuated domains enriched in both Av-GPI and CTxB-labeled GM1 (Figure 7A) (70).

Contrary to the lovastatin experiment, mβCD treatment induced a significant reduction in Av-GPI lateral mobility. SQT analysis showed a single distribution of diffusion coefficients (Figure 7 C) with a modal value nearly three times smaller than the slow Av-GPI subpopulation in untreated cells ($\hat{D}^{+m\beta CD-CT\times B} = 3.5 \times 10^{-4}$ μm²/ s versus $\hat{D}^{-CT\times B}_{slow} = 9.1 \times 10^{-4}$ μm²/ s). Concomitantly, the typical corral radius of confined diffusions was reduced from 152

to 72 nm (SE 64–80 nm, $n = 17$, data can be viewed at http://fpinaud.bol.ucla.edu/index_files/Traffic.htm). This reduction in lateral mobility was confirmed by FRAP, but mobility could be restored to pretreatment levels after incubation in serum-supplemented media for 20 h (Figure 7B).

The reduction in Av-GPI surface density, together with the loss of the fast diffusing population and the presence of a single and slow regime of diffusion suggested that most Av-GPI in the membrane might be associated with GM1-rich domains after mβCD treatment. To test this hypothesis, we repeated the SQT experiments in the presence of Alexa 488-CTxB. The number of GM1-rich microdomains in mβCD-treated cells was much lower than those observed for untreated cells and the mobility of CTxB-labeled GM1 appeared reduced (Video 9). More than 50% of all qdot-labeled Av-GPI colocalized with stationary GM1-rich microdomains (Figure 7D), and CTxB labeling further reduced their mobility, essentially bringing them to a halt ($\hat{D}^{+m\beta CD+CT\times B} = 2.7 \times 10^{-5}$ μm^2/ s $< D_{min} = 4.8 \times 10^{-5}$ μm^2/ s, Figure 7 C). This observation is therefore consistent with most of the Av-GPI being associated with GM1-rich microdomains after cholesterol depletion by mβCD.

We then repeated the mβCD treatments on HeLa cells coexpressing Av-GPI and Cav1-EGFP. As before, a single population of slow Av-GPI was observed (data not shown). Av-GPI mostly localized in close proximity to immobile Cav1-EGFP-labeled membrane domains (Figure 7D). Because we previously showed that Av-GPI diffusing in GM1-rich microdomains tend to localize close to caveolae, finding Av-GPI in close proximity to Cav1-EGFP-labeled structures after mβCD treatment further supports our observation that Av-GPI are mainly associated with GM1-rich regions of the membrane after acute cholesterol depletion.

Actin cytoskeleton disruption results in faster Av-GPI diffusion but does not suppress slow diffusion

The cortical actin meshwork is essential in maintaining cell shape and structure by providing a dynamic and elastic scaffold to the plasma membrane (71). The actin cytoskeleton can also influence the surface topology of the plasma membrane and affect the diffusion of raft-associated lipids and proteins involved in signaling (72,73). To evaluate the role of the actin network, we studied the diffusion of Av-GPI and GM1 after treatments of HeLa cells with a high concentration of latrunculin-A, a potent actin-disrupting agent (74) (Figure S10 and discussion in Supporting information). Despite extensive disruption of F-actin with 10 μM latrunculin-A, we still observed fast- and slow-diffusing populations of Av-GPI (Video 10). However, membrane retraction and ruffling induced by extensive actin depolymerisation prevented us from studying the correlation between slow Av-GPI diffusion and the proximity of GM1-rich domains. Because of this altered topology of the membrane, we only studied trajectories that did not get close to these perturbations and limited our analysis to reporting the diffusion coefficient of fast Av-GPI only. The diffusion coefficient of fast Av-GPI ($\hat{D}^{lat\text{-}A}_{fast} = 1.7 \times 10^{-1}$ μm^2/ s, SE: $1.4 - 2.1 \times 10^{-1}$ μm^2/ s) increased nearly fivefold compared to untreated cells, suggesting that the cortical actin cytoskeleton can impend the diffusion of fast Av-GPI in normal conditions. This diffusion coefficient was similar to that of qdot-labeled Av-GPI diffusing in the L_d phase of 1:1 DPPC:DOPC + 0.01% fluorescein-DPPE-supported lipid bilayers within which the GPI-test probes were reinserted after extraction from the membrane of HeLa cells (data not shown). Interestingly, however, the observation that many Av-GPI (∼ 50% of traces) still diffused slowly in live cells indicated that an intact actin cytoskeleton was not necessary for the existence of slow diffusion domains in the membrane.

Discussion

Considering the complex, crowded and dynamic architecture of cell plasma membranes, it can be challenging to assess how different membrane components affect the diffusion of endogenous proteins or lipids. The task is even more complicated without a complete map of existing interactions between these molecules. In this respect, tracking exogenous probes can be advantageous in deciphering the respective influence of protein- or lipid-based microdomains, of membrane heterogeneous scaffolding or of the extracellular matrix on the lateral mobility of biomolecules. By designing a raft-associated GPI-anchored test probe (Av-GPI) having no biological function and no specific interaction with other proteins (but possibly non-specific ones), we aimed to study the organization of the plasma membrane and in particular the influence of lipid raft microdomains on the diffusion of raft-associated proteins in HeLa cells. Using targeted qdots and single-molecule imaging techniques, we studied the long-term diffusion of Av-GPI and revealed the existence of non-caveolar, cholesterol- and GM1-rich microdomains within which these GPI-anchored probes can dynamically partition and be compartmentalized.

Av-GPI as a raft-associated GPI-AP model probe

We showed that Av-GPI is efficiently expressed and targeted to lipid rafts as defined biochemically (Figure 1). As commonly observed for native GPI-AP, (i) Av-GPI associates with DRM in a cholesterol-dependent manner (Figure 1C), (ii) colocalizes with GM1 patches induced by antibody cross-linking (Figure 1B) and (iii) diffuses with diffusion coefficients typical of GPI-AP in HeLa cells (56). Thus, Av-GPI appears to be an appropriate model probe to study the dynamics of raft-associated GPI-AP in this cell type.

Because avidin form tetramers in solution, the choice of Av-GPI as a model GPI-AP may appear problematic as it could exist in various multimeric forms in the membrane (monomer, dimer, etc), each characterized by

a different diffusion behavior. We have shown, however, that Av-GPI is displayed in the cell membrane as a tetramer, rather than as a mixture of monomers, dimers, trimers or higher-order oligomers (such as multitetramers). In addition, we minimized the probability of targeting hypothetical non-tetrameric configurations of Av-GPI by using concentrations of biotinylated qdots ($\sim 10^{-12}$ M) well below the K_D of the monomeric ($K_D \sim 10^{-7}$ M) and dimeric ($K_D \sim 10^{-8}$ M) forms of avidin (75,76). Finally, the size variation between a monomer and a tetramer (or for that matter multitetramers) cannot account for the observed 1–2 orders of magnitude variation in diffusion coefficients (77). Thus, heterogeneous multimerization of Av-GPI, even though it is possible in principle, cannot explain the two main diffusion regimes we observed.

Small peptide-coated qdots have limited effects on the intrinsic diffusion of Av-GPI

We further demonstrated that the valency of biotinylated qdots had little effect on the diffusion of Av-GPI and did not induce their cross-linking and slowing down in the membrane, even when 50% of the coated peptides were biotinylated (Figure S3). We did not test higher valency because we previously showed that excessive amount of biotin on the qdot surface can inhibit the binding to Av-GPI owing to steric hindrance (43). This valency-independent behavior is in stark contrast with that of antibody-coated gold particles commonly used for SPT, where diffusion differs depending on whether quasi-monovalent or multivalent particles are used (78,79) or whether free ligand is added to cells during tracking (80). In the case of multivalent particles, cross-linking of several proteins to a single gold probe is possible because of the large size of the particle and the recognition of surface epitopes; two problems eliminated by the small size of peptide-coated qdots and the reduced accessibility to the deeply buried biotin-binding pockets of GPI-anchored avidin. The absence of qdot-induced transient or permanent clustering of Av-GPI was further confirmed by SDT and FRAP with monovalent biotinylated probes. As a result, we deem it unlikely that the slow-diffusing population of Av-GPI corresponds to transient anchorage (81) or to stimulation-induced temporary arrest of lateral diffusion (80).

Comparison between SQT, SDT and FRAP experiments also revealed a twofold reduction in the diffusion coefficient of Av-GPI when labeled with qdots. Similar differences have been observed for SPT with gold nanoparticle probes (33). Although these differences have been attributed to the valency and size of SPT probes (33), our data with quasi-monovalent qdots point toward a size effect only. Despite their small size ($\sim$ four times smaller than antibody-labeled gold nanoparticles), peptide-coated qdots may still interact with the immediate membrane environment, especially when imaging is performed in the ventral membrane. However, the characteristic multimodal diffusion of Av-GPI was not an artifact of qdots, because quantitatively similar changes in diffusion were still observed with smaller and monovalent fluorescent probes. Despite carrying a qdot, diffusing Av-GPI were still able to access very small membrane structures such as caveolae. Using small peptides to functionalize qdots minimizes their final size and cross-linking issues and thus provides a very advantageous alternative to streptavidin and antibody-functionalized qdot or gold probes.

Av-GPI dynamically partition in stationary GM1-rich domains in the membrane of HeLa cells

Our analysis showed that the diffusion of Av-GPI in the membrane of HeLa cells is heterogeneous and is characterized by a broad, bimodal distribution of diffusion coefficients (Figure 3). The diffusion coefficients determined here by SQT, SDT and FRAP are well within the range reported for various GPI-AP (10^{-4} to 25×10^{-2} $\mu m^2/s$) (33). The presence of diffusion regimes differing by 1–2 orders of magnitude has also been previously reported for other GPI-AP such as Thy-1 (82,83), NCAM120 (84), or GPI-modified MHC class II proteins (85), but the origin of the observed slow diffusion has remained unclear. Here, using CTxB as glycosphingolipid GM1 marker and Cav1-EGFP as a caveolae marker, we provide direct evidence that slow Av-GPI diffusion correlates with entry into or interaction with stationary, non-caveolar GM1-rich microdomains. Fast Av-GPI diffusion, however, mainly takes place in what appears to be a continuous phase where GM1 also diffuse rapidly. The simultaneous colocalization and slow diffusion of two ''raftophilic'' molecules (Av-GPI and GM1) in membrane domains separated from an apparently more fluid membrane phase strongly suggest that GM1-rich microdomains might harbor putative lipid rafts, regardless of their actual size. The existence of two main diffusion regimes for Av-GPI correlating with these different membrane domains further indicates that, in HeLa cells, GM1-rich microdomains are capable of influencing the partitioning and the diffusion of membrane proteins, independently of protein multimerization or probe cross-linking.

It is worth mentioning here that the existence of these two different diffusion regimes is not an artifact of the 100 ms/frame rate used in these experiments. Although long duration fast diffusions observed at slow frame rates may result in blurring of the qdot's point spread function (PSF), the centroids of these (potentially but not necessarily) blurred PSFs can still be accurately determined. Indeed, it has been previously demonstrated by Monte Carlo simulations that frame rate does not affect the determination of diffusion coefficients for uniform Brownian diffusion (35). Our choice of frame rate does not allow us to detect random alternation of very brief bursts of fast diffusion (<milliseconds to a few milliseconds) described in much faster tracking studies (35). It is thus possible that either or both the fast- and slow-diffusion regimes of Av-GPI identified in this study may in fact comprise very short phases of very rapid diffusion. However, such a behavior would only increase the measured average diffusion coefficients for each regime, without

changing the fact that there are two typical diffusion regimes. Thus, as proposed in the lipid raft hypothesis (25), GM1-rich microdomains compartmentalize the diffusion of Av-GPI, as we observed at both room temperature (~ 27°C) and 37°C (SQT, Figure 3A and data avaible at http://fpinaud.bol.ucla.edu/index_files/Traffic.htm).
Although our analysis did not distinguish between corralled diffusion and diffusion limited by obstacles, the colocalization of slow diffusion regimes with CTxB-labeled regions suggests an effective compartmentalization in GM1-rich microdomains (radius: 152 nm). On the other hand, GM1-rich regions also appear in some cases to act as barriers to the diffusion of fast Av-GPI. The observation of trajectories grazing without entering these regions suggests that the characteristic length scale of restricted diffusion for fast Av-GPI (radius: 640 nm) reflects the characteristic distance between discontinuous GM1-rich microdomains. As emphasized previously, this compartmentalization effect is independent of CTxB labeling (Figure 3A) but appears accentuated in the presence of the toxin subunit.

The observation of stationary GM1-rich microdomains and mobile GM1 sphingolipids, both labeled with CTxB, is consistent with several previous studies. FRAP measurements on cell membranes have shown that an immobile fraction of CTxB-labeled GM1 coexists with rapidly diffusing GM1-associated CTxB (86). FRET measurements in live cells also demonstrated that CTxB can bind both clustered and non-clustered GM1 (87). The existence of stable GM1-rich microdomains in the absence of CTxB has also been confirmed by freeze fracture electron microscopy (88). These experiments provided initial evidence that GM1 clustering is not simply a function of CTxB binding, and that CTxB can effectively be used to detect preexisting GM1-rich microdomains.

Still, CTxB can induce subtle changes in GM1-rich microdomains, which are consistent with GM1 clusters being stabilized upon binding of the pentameric toxin subunit in these domains (87). We observed that CTxB labeling leads to (i) an ~threefold increase in immobile Av-GPI, (ii) an ~fourfold reduction in the diffusion coefficients of the slow population and (iii) an ~twofold reduction in the corral size for the slow confined subpopulation. These changes might stem from partial cross-linking of small GM1-rich structures by CTxB (29,88). Alternatively, they may simply reflect a contraction of preexisting large microdomains because of the replacement of free GM1 molecules by denser GM1-CTxB clusters. In both cases, clustering of GM1 lipids creates an obstacle-rich environment for slow Av-GPI and leads to even slower diffusions or immobilization. CTxB-stabilized structures also appear less permeable to the diffusion of fast Av-GPI as observed from the ~1.5-fold reduction in characteristic confinement size for the fast confined population. Both effects can explain the reduced dynamic partitioning of Av-GPI in and out of GM1-rich microdomains observed after addition of CTxB (11% of all Av-GPI versus 22% when CTxB is omitted). Indeed, obstructed diffusion and slowing down of Av-GPI within CTxB-labeled GM1-rich microdomains could result in a lower escape probability (transition from slow to fast), while the reduced permeability could lead to a lower probability to enter them (transition from fast to slow).

Thus, CTxB induces subtle changes in the organization of GM1-rich microdomains, which can then influence the diffusion of GPI-AP. It is then important to consider these effects when studying the organization of cells plasma membrane. The influence of CTxB on the diffusion of Av-GPI and its recently demonstrated ability to induce the coalescence of raft-like membranes microdomains (89) can be exploited to highlight preexisting putative raft microdomains. These effects, however, also limit the use of CTxB to study the diffusion of GM1 lipids.

Two additional observations may give clues about the organization of GM1-rich domains: (i) some fast Av-GPI were observed to diffuse through CTxB-labeled domains without slowing down (Figure 3D; Figure S9C) and (ii) the largest fraction of slow Av-GPI did not exhibit any confinement. Highly dynamic barriers delimitating GM1-rich microdomains could account for these characteristics. Alternatively, they fit well into a lipid raft model that predict them to be small (10–200 nm, bellow optical resolution) (25) and capable of forming high-density nanodomains (<10 nm) stabilized by cholesterol and sphingolipids (6,90). GM1-rich microdomains might thus be interpreted as regions with higher local density of nanodomains than the rest of the plasma membrane. In these regions, slowing down of Av-GPI could be the result of increased interaction with such nanodomains (91,92).

The fact that Av-GPI transiently interact with glycosphingolipid-rich microdomains indicates that the dynamic partitioning raft model (83,86) is appropriate to describe the diffusive behavior of this GPI-AP in HeLa cells. This partitioning in and out of GM1-rich microdomains was similar for two HeLa cell lines having 10-fold differences in Av-GPI membrane expression levels (data can be viewed at http://fpinaud.bol.ucla.edu/index_files/Traffic.htm). This suggests that the membrane partitioning of GPI-AP is maintained independently of the protein expression levels. As discussed below, membrane lipids and, in particular, cholesterol and glycosphingolipid GM1 might be important regulators of this partitioning.

Caveolae and GM1-rich domains are distinct membrane structures

Two independent observations indicate that GM1-rich domains and caveolae, despite their known similar raft-like composition, are related but distinct structures of the membrane in HeLa cells. First, two-color imaging and SQT of Cav1-EGFP and qdot-labeled Av-GPI showed that, in most cases, transition from fast to slow diffusion was not caused by entry into caveolae. However, many SQT trajectories exhibited a fast-to-slow transition

within a few hundred nanometers of caveolae. Second, although confocal imaging of caveolae and cross-linked Av-GPI indicated a statistically significant proximity of the GPI probes with caveolae, they did not significantly colocalize. This observation might be cell-type specific, as the literature contains results supporting as well as contradicting it. For instance, our confocal microscopy observations seem in agreement with a study of BHK cells showing that cross-linked GPI-anchored placental alkaline phosphatase does not result in accumulation into caveolae (50), but in contradiction with other studies reporting enrichment of GPI-AP in caveolae after cross-linking (93,94).

Although caveolae and GM1-rich domains appear morphologically distinct, their observed proximity (Figure 6) is consistent with various functions attributed to caveolae. It has recently been suggested that caveolae play a role in lipid regulation, via the interaction of caveolin-1 with cholesterol, by acting as cholesterol and sphingolipid reservoirs and regulating their supply to membrane raft (95). The proximal localization of GM1-rich microdomains with caveolae observed here in live cells is reminiscent of other reports in which GPI-AP-rich membrane microdomains were found adjacent to caveolae (59,96,97). This close proximity could facilitate cholesterol and GM1 exchange between the two compartments.

We did not investigate the relation between GM1-rich microdomains and clathrin-coated pits in this study. Previous reports have indicated that GM1 and some GPI-AP interact with clathrin-coated invaginations (98–100), but a study using FRET and immunofluorescence has clearly shown that CTxB-labeled GM1 clusters are excluded from them (87). Because we showed that slow diffusing Av-GPI are colocalized with GM1-rich domains, it is unlikely that slow diffusion is due to interaction with clathrin-coated pits. Further study will be needed to fully address this question.

Slow diffusion of Av-GPI may also be the result of entry into CTxB-labeled membrane invaginations other than caveolae or clathrin-coated pits, such as clathrin-independent carriers (101,102). Such carriers can transport GPI-AP and GM1 toward GPI-AP-enriched endosomal compartments (103). We have not tested this possible relationship, but one observation argues against it. Indeed, caveolin-1 expression was reported to reduce the endocytic efficiency of clathrin-independent carriers (101). Since different expression levels of caveolin-1 (between the cell line not expressing Cav1-EGFP and that expressing it) did not significantly affect the bimodal distribution of Av-GPI in HeLa cells, slow Av-GPI do not seem to interact significantly with such invaginations.

Cholesterol regulates the organization of GM1-rich domains and the dynamics of Av-GPI

We showed that two standard cholesterol-depleting drugs have very different effects on the diffusion of Av-GPI. Lovastatin treatments, which mildly modified the actin cortical network (Figure S8A) barely changed cellular and plasma membrane cholesterol levels or the distribution of GM1 in the membrane (Figure S8B). Accordingly, the diffusion of Av-GPI and GM1 was not significantly affected. mβCD had similar effects on the cytoskeleton, but led to markedly reduced cholesterol and GM1 membrane levels. Concomitantly, the fast population of Av-GPI was strongly affected and our test probes appeared mainly associated with GM1-rich microdomains. This mβCD treatment not only led to a significant reduction in the lateral mobility of Av-GPI but also of GM1, as observed for other GPI-AP and glycosphingolipids in previous studies (87,104,105). Despite the possible indirect effects of mβCD treatment on the actin cytoskeleton (106), changes in the diffusion of Av-GPI and GM1 observed in mβCD-treated cells, but not in lovastatin-treated cells, appear mainly owing to the altered cholesterol and GM1 membrane levels rather than to a reorganization of the actin cytoskeleton. A similar dependence of the mobility of GM1 and other GPI-AP on membrane cholesterol content, but not on actin, was recently observed in COS-7 cells using FCS (30) and in CHO cells by single-dye tracking (104). We also observed a reduced mobility of Av-GPI after mβCD treatment by FRAP. These FRAP experiments, which were performed with much higher concentrations of biotinylated probes compared to that used for SQT, showed that not only did the fraction of immobile Av-GPI increase dramatically but also that a significant fraction still diffused over long distances (Figure 7B). This apparently contradicts the fact that we rarely observed trajectories extending beyond 1 μm during SQT. However, the two observations can be reconciled if the apparent enrichment of Av-GPI within GM1-rich domains after mβCD treatment simply reflects higher number of Av-GPI within these domains compared to the rest of the membrane. In this case, random binding of the few qdots used for SQT will preferentially take place in these domains. This hypothesis is in agreement with the punctuated membrane distribution and the colocalization of Av-GPI with GM1 domains observed by confocal microscopy at high concentration of probes (Figure 7A). If, as it appears, these domains cover only a small fraction of the total membrane surface area after mβCD treatment, their contribution to the total fluorescence intensity monitored by FRAP is expected to be moderate, as observed in practice.

There could be several causes to such an apparent enrichment of Av-GPI in GM1-rich microdomains upon acute membrane cholesterol depletion. Changes in the lipid composition of microdomains could result in higher affinity of Av-GPI for these regions compared to the rest of the membrane and lead to an effective accumulation by altered partitioning. Alternatively, extending the argument used to interpret the decrease in dynamic partitioning in and out of GM1-rich microdomains after CTxB labeling, the apparent enrichment could be simply due to longer time spent in GM1-rich domains. Observing

even longer trajectories than observed here may allow testing this hypothesis in future experiments. Finally, our data might reflect the action of mβCD on different membrane cholesterol pools. It has been shown that mβCD preferentially disrupts glycerophospholipid-rich regions in plasma membranes and spares sphingolipid-rich microdomains (66). In these domains, cholesterol can tightly pack against the hydrocarbon chains of sphingolipids and can be shielded from extraction. The same report also showed that removal of membrane cholesterol by mβCD can indirectly induce the release of GPI-AP not associated with glycosphingolipid-rich domains. Under similar conditions, we also observed a reduction in the Av-GPI surface density by FACS and confocal imaging, as well as the presence of a single Av-GPI population associated with GM1-rich microdomains. It is thus possible that Av-GPI that are not associated with sphingolipid-rich microdomains (fast population) have been preferentially extracted following cholesterol removal by mβCD, while Av-GPI associated with GM1-rich microdomains (slow population) were spared. The unbalanced membrane distribution of Av-GPI induced by such a differential effect of mβCD can explain why the population of Av-GPI associated with GM1-rich microdomains appears enriched after cholesterol depletion. Importantly, such an effect supports our finding that Av-GPI can reside and dynamically partition in two plasma membrane lipid phases having different glycosphingolipid GM1 organization and different cholesterol contents.

We also showed that the characteristic size of GM1-rich microdomains, as well as the diffusion coefficients of Av-GPI in these domains, was reduced after acute cholesterol depletion with mβCD. Both effects are consistent with an increased ordering of glycosphingolipid GM1 around Av-GPI in these regions and could reflect a transition from an L_o phase toward a gel (solid-like) lipid phase, favored at low membrane cholesterol and GM1 concentrations (107,108). A similar transition was recently reported by Nishimura et al. (105). The near complete immobilization of Av-GPI after addition of CTxB (Figure 7, ~80—fold decrease in $\hat{D}$ for mβCD-treated cells versus ~3-fold decrease for untreated cells) also suggests that cholesterol depletion induces a high density packing of GM1 around Av-GPI in GM1-rich microdomains, which is compounded by a more efficient cross-linking of GM1 by CTxB.

Together, these results indicate that an appropriate balance between cholesterol, GM1 and other membrane lipids is essential for the fluidization of GM1-rich microdomains and for the membrane distribution of both Av-GPI and GM1. They attest that cholesterol is a key element for the dynamic of raft-associated biomolecules and for the organization and maintenance of some sphingolipid-rich microdomains.

Slow diffusion of Av-GPI is not induced by actin-stabilized microdomains

Recent studies have suggested that the cortical actin cytoskeleton modulates the diffusion dynamics of outer membrane protein and lipids by (i) organizing the plasma membrane in small and juxtaposed domains delineated by transmembrane proteins anchored to the underlying actin network (picket-fence model) (8) and (ii) stabilizing cholesterol-dependent clusters of raft-associated proteins following cross-linking in transient confinement zones (TCZs) (84,109), transient anchorage zones (TAZ) (81) or zones of stimulation-induced temporary arrest of lateral diffusion (STALL) (80). In line with some of the predictions of the picket-fence model, we find that extensive disruption of the actin cytoskeleton results in significantly faster diffusion of fast Av-GPI. Surprisingly, however, many slow-diffusing Av-GPI could still be observed, an indication that domains of slow diffusion, which our study strongly correlated with GM1-rich microdomains, are not directly maintained by the actin cytoskeleton. A similar observation has been recently reported by Lenne et al. (30). These actin-independent microdomains in which Av-GPI experience slow diffusion seem distinct from actin-stabilized membrane domains such as TCZs, which have been observed for a variety of GPI-AP including Thy-1, NCAM125 and CD59 (80,84,109). TCZs, TAZs and STALLs zones are thought to be membrane domains enriched in glycosphingolipids (83), in which GPI-AP can be efficiently cross-linked. In short, they are regarded as ''cluster-stabilized'' lipid rafts. As observed for TCZs, the confinement size of slow Av-GPI is on the order of 300 nm in diameter, is cholesterol-dependent and is reduced twofold after mβCD treatments. As for TCZs, domains of slow diffusion can also be revisited and Av-GPI can diffuse within them for tens of seconds. Thus, there are some parallels between the membrane microdomains where Av-GPI diffuse slowly and TCZs observed for other GPI-AP. However, one major difference is that, in contrast to our measurements, TCZs are detected after cross-linking and clustering of raft-associated molecules by multivalent gold particles (5). Accordingly, the lifetime and diffusion coefficients of TCZs depend on the number of molecules that are cross-linked (78,81). The large size of the gold probes might also lead to non-specific binding to other membrane proteins or lipids, which could result in an overestimation of confinements. Here, we have shown that with small and quasi-monovalent probes, a GPI-AP can display zones of slow diffusion that share many characteristics of TCZs, but are detected in the absence of cross-linking. Moreover, we did not find any correlation between the time spent by Av-GPI in GM1-rich domains and the qdot probes valency. Furthermore, Av-GPI with restricted diffusion represent only a small fraction of all slow Av-GPI, as expected for domains that are not induced by cross-linking. Finally, diffusion in TCZs is characterized by diffusion coefficients that are only about twice as smaller to those outside TCZs, while we find much larger variation of diffusion coefficients (~40-fold) when Av-GPI partition in and out of GM1-rich microdomains.

Thus, our data supports the presence of preexisting membrane microdomains having characteristics similar to that of putative lipid rafts and capable of influencing the partitioning and the diffusion of GPI-AP, independently of probe cross-linking and stabilization by the actin cytoskeleton. It is, of course, possible that these same microdomains become transient confinement zones after cross-linking. More experiments with better control on decoupling the cytoskeleton from the membrane will be needed to fully elucidate the relationship between GM1-rich microdomains, slow-diffusing GPI-AP and the cytoskeleton.

Conclusion

We have developed two HeLa cell models expressing an artificial GPI-AP to address the nature and dynamics of putative raft microdomains in the membrane of living cells using long-term single-qdot tracking. According to a recent review, lipid rafts are expected to be 'small (10–200 nm), heterogeneous, highly dynamic, sterol- and sphingolipid-enriched domains that compartmentalize cellular processes. Small rafts can sometimes be stabilized to form larger platforms through protein/protein and protein/lipid interactions' (25). Using both Av-GPI and CTxB as raft markers and Cav1-EGFP as a caveolae marker, we have shown that the diffusion of raft-associated proteins is indeed highly dynamic and heterogeneous. In particular, the diffusion of Av-GPI was slowed down upon interaction with stationary GM1-rich microdomains, which were often found in proximity to caveolae but distinct from them. The slow and cholesterol-dependent diffusion of Av-GPI in sphingolipids GM1-rich microdomains further indicates that these membrane regions can compartmentalize cellular processes and are potential lipid raft sites. The cross-linking and crowding effects of CTxB also indicates that GM1 is enriched in GM1-rich microdomains and that these domains can be stabilized by specific protein/lipid interaction. Our data further demonstrates that the dynamic partitioning raft model satisfactorily describes the diffusive behavior of some raft-associated proteins into and out of GM1-rich microdomains in live cells.

Although our results are currently limited to a single cell type, they support the raft hypothesis by providing direct evidence that a GPI-AP can dynamically partition and be compartmentalized in non-caveolar, cholesterol- and GM1-rich microdomains in the plasma membrane of living cells.

Materials and Methods

Single-molecule imaging by objective-type TIRF

Custom-built dual-color TIRF microscopes were used to perform two-color imaging of qdot-labeled Av-GPI and CTxB Alexa 488 labeled-GM1 or Cav1-EGFP (schematics can be viewed at http://fpinaud.bol.ucla.edu/index_files/Traffic.htm). In both cases, the ventral plasma membrane of HeLa cells was imaged. The diffusive behavior of Av-GPI was similar in the ventral or dorsal membrane (data not shown). However, we preferred ventral imaging by TIRF to limit the probability of imaging membrane regions containing microvilli or other membrane corrugations, thus guaranteeing that the diffusion of the Av-GPI was essentially confined in two dimensions (110). A detailed description of the setups is available in Supporting Information. Unless stated, imaging was done at room temperature ($\sim 27^{\circ}$C).

Typically, two to three cells per field-of-view were imaged continuously for 90–120 s, using an integration time of 100 ms per frame. Faster acquisitions were also performed (7 ms/frame using only a subset of the EMCCD camera, data not shown). However, because of software limitations that prevented from storing movies with large numbers of frames, such faster frame rate would have resulted in trajectories with shorter duration (and limited field of view), which would have undermined our ability to detect the existence of long-term changes in diffusion regime in the cell membrane. In addition, because CTxB-Alexa 488 and qdots have different brightness, acquisition times had to be optimized so that both signals could be simultaneously detected on each side of the same EMCCD camera. At 100 ms/frame, there was a good balance between signal intensity and acquisition speed.

For single-dye tracking (SDT) of Av-GPI labeled with Alexa-488 biocytin (Invitrogen), imaging was performed continuously with an integration time of 60 ms and at a final dye concentration of 75 pM. For all conditions, cells grown at $\sim$ 70% confluency on fibronectin coated coverslips were first starved for 3–4 h in serum-free DMEM at 37°C to free Av-GPI from biotin present in the serum supplement. Cells were then imaged in HBSS + 1% BSA for a maximum of 30–45 min after which they were replaced.

Biotinylated CdSe/CdS/ZnS qdots emitting at 620 nm and coated with 50% biotinylated peptides and 50% of 600 Da polyethylene glycol (PEG) peptides were synthesized and prepared as previously described (43,111). Alternatively, 620 nm–emitting CdSe/ZnS in toluene (Evident Technologies, Troy, NY) were used and coated with peptides as above. The final diameter of the biotinylated qdots was 13.0 ± 1.1 nm (112). Quasi-monovalent biotinylated qdots were obtained by reducing the amount of biotinylated peptides to 1–2% during the coating procedure and using 49–48% of a third, lysine-terminated peptide (peptide #7 in Pinaud et al. (43), Figure S3). Qdots were added to the cells at a final concentration of 2–3 pM directly in the imaging media to label only few Av-GPI ($\sim$10 per cell). A low-level labeling facilitated tracking for long duration by limiting the probability that two or more qdot-labeled Av-GPI crossed paths or blinked simultaneously within the same area. In addition, low concentrations of qdots limit potential toxic effects (113) and interference with normal cellular metabolism. For dual-color imaging experiments, a final concentration of $0.05 - 0.1$ μg/mL of Alexa 488 cholera toxin B (CTxB) was added simultaneously with qdots.

Data analysis

Post-acquisition, each frame of a recorded TIRF movie was split into two images (green and red channels) using Metamorph software (Molecular Device, Sunnyvale, CA). Images of both channels were overlaid after correcting for offsets and spherical and chromatic aberrations as determined from the emission of 40 nm TransfluoSpheres. A software was developed in Labview (National Instruments, Austin, TX) to track and analyze trajectories of qdot-labeled Av-GPI (See Supporting information for details). Briefly, regions of interest in images were selected and a semiautomatic algorithm was used to fit the point-spread-function (PSF) of the tracked qdots with a 2D Gaussian in each frame (52,53) (Figure 2). The quality of the fit was verified visually for each frame. When the signal in a frame was lost because of blinking, no fitting was performed until reappearance of the PSF. When a PSF did not reappear within 10 s, tracking was aborted. Tracking was also aborted when two qdot-labeled Av-GPI crossed paths. Because of blinking, binding to cell membrane during imaging, or internalization of qdot-labeled Av-GPI, the mean duration of trajectories varied between 50–75 s. After tracking, a trajectory file containing all information was saved for each Av-GPI molecule. Subsequent analysis (described in detail in Supporting

Information) included (i) computing the mean-square displacement (MSD) curve for a trajectory, (ii) representing the fluorescence intensity along the diffusion path, (iii) representing the instantaneous diffusion coefficient (38), (iv) calculating the probability distribution of square displacement $P(\bar{r}^2, \tau)$ (PDSD) for each molecule or for all molecules by global analysis (55) and (v) analyzing PDSD for different time lags in terms of diffusion models (Table S2). The presence of single or multiple diffusive regimes within each trajectory was deduced from PDSD analysis on the first 10% of time lags t, and by fitting the PDSD with one, two or three exponentials. The quality of each fit was evaluated using the normalized residual curve. Normalized residuals deviating systematically by more than 10% (from zero) resulted in the rejection of the fitted curve. The fitted exponents obtained were then used to plot $r_i^2(t)$ curves for different time lags t (see Supporting Information). If the PDSD curves were well fitted with a single exponential, the corresponding single $r^2(t)$ curve was plotted (Figure 2D, Av-GPI with a single diffusion mode). If the PDSD was best fitted with more than one exponential, then as many $r^2(t)$ curves were plotted (Figure 2D, Av-GPI with multimodal diffusion). For each $r^2(t)$ curve, the diffusion mode and corresponding diffusion coefficient were determined as follows. The diffusion model that best described an $r^2(t)$ curve was selected by fitting the $r^2(t)$ curve with the most likely among diffusion models picked from Table S2. For instance, for a concave $r^2(t)$ curve, we skipped the directed motion model. The respective quality of each fit was assessed visually, although a quantitative method such as normalized residuals analysis could be implemented if needed. Additionally, we used Occam's razor principle, keeping the model with the least parameters if two or more models accounted well for the $r^2(t)$ curve. The fitting parameters for the best fit diffusion model were used as is (see Supporting Information). This approach does not only permit a classification of each mode of diffusion into pure Brownian, restricted or directed motion as does the approach of Wilson et al. (114) but also allows the computation of a diffusion coefficient for each mode. Since the PDSD curves are calculated for the first 10% of time lags, there is ample statistics to obtain reliable $r_i^2(t)$ curves. Monte Carlo simulations of trajectories of freely diffusing particles, confined or switching between free and confined diffusion, confirmed that PDSD analysis could detect multimodal diffusion and correctly recover the diffusion coefficient for each mode of diffusion (Figure S5). In few cases, no convincing PDSD fits or no convincing $r^2(t)$ fits could be obtained. In these cases, the trajectories were rejected.

In addition to the classification into different mode of diffusion, we identified a category of immobile Av-GPI (if $D < D_{\text{min}}$) using a diffusion coefficient threshold $D_{\text{min}} = 4.8 \times 10^{-5}$ μm^2/s. This cut-off value D_{min} corresponds to the 95th percentile of the distribution of diffusion coefficients for qdots imaged on fibronectin-coated coverslips, and represents the level of drift in the setups (Figure 3, gray histogram).

The apparent diffusion coefficients measured from fitting each $r^2(t)$ curve were reported in histograms. Because the diffusion coefficients are distributed log-normally over several orders of magnitudes, histograms of the decimal logarithms of diffusion coefficients are reported (D-histograms in the following). The bin size of the D-histograms was determined statistically using an approach introduced by Knuth (115). This method adapts the bin size to the underlying distribution without a priori knowledge of its nature. After evaluating the optimal bin size for each experimental condition, we chose twice the largest bin size and applied this modified optimal bin to all data. With this common bin size, a direct comparison between all distributions is possible, and subpopulations in histograms are sufficiently separated.

In the text, the diffusion coefficients reported correspond to the peak position(s) of single (or multiple) Gaussian fit(s) of the D-histograms. Standard errors values (SE) were determined using 1000 bootstrap replica of the distributions (116) and are given in the form of an upper and lower diffusion coefficient. Because the distributions of the diffusion coefficients are relatively large, we only considered differences in diffusion coefficients larger than three times the SE to be significant.

To evaluate the number of Av-GPI switching between the fast and slow regime (or vice versa), a cut-off value corresponding to the 95th percentile of the Gaussian fitted on the slow distribution was used (e.g. 1.3×10^{-2} μm^2/s for Figure 3A). Av-GPI trajectories having two very different diffusions regimes distributed above and below this cut-off value were classified as switching trajectories.

The sizes of confinement domains are extracted for Av-GPI traces fitted with a restricted diffusion model (Table S2) and are separately determined for fast and slow subpopulations. The confinement/zone geometry is assumed to be circular (corral). As for diffusion coefficient values, corral sizes appeared to be distributed log-normally. We therefore computed histograms of decimal logarithm of sizes. Confinement sizes were determined by Gaussian fitting of the distribution histograms. Standard error of the mean (SE) was determined as before. Differences in confinement size larger than three times the SE were considered to be significant.

To study the colocalization of Av-GPI with immobile/slow diffusing CT×B-labeled GM1-rich domains or Cav1-EGFP-labeled caveolae, Av-GPI trajectories were overlaid with the mean intensity projection image of the movie (green channel, $\sum I_{\text{mean}}$). $\sum I_{\text{mean}}$ is defined as the image whose pixel value $p(k, l)$ at coordinates (k, l) is the mean value of all pixels $p_i(k, l)$ for N frames of the movie at this location:

$$p(k, l) = \frac{1}{N} \Sigma_{i=1}^{N} p_i(k, l). \quad (1)$$

With this approach, diffusing GM1 or Cav1-EGFP are efficiently filtered out from the final image and GM1-rich microdomains and caveolae are easily identified (data can be viewed at http://fpinaud.bol.ucla.edu/index_files/Traffic.htm). Further confirmation of colocalization was done by overlaying the fluorescence intensity time trace of a qdot-labeled Av-GPI along its trajectory (in a 3×3 pixel region centered on the qdot location) with the corresponding fluorescence intensity time trace in the green channel. Periods showing overlap of red and green fluorescence after background subtraction were interpreted as interaction of Av-GPI with GM1 domains or caveolae. However, this approach is limited by the bleaching of organic dyes and EGFP, which make the distinction between labeled and non-labeled regions more difficult at longer times. In few cases, we could correlate changes in diffusion (D_{in} and D_{out}) with the entry or exit from GM1-rich domains or caveolae by performing MSD analysis on subtrajectories and PDSD analysis (Figure S5). Parts of the trajectory in which Av-GPI is colocalized with a GM1-rich domain or a caveola (identified by fluorescent signal above background in the CTxB or Cav1-EGFP channel) were selected and separated from the non-colocalized parts. The MSD of each subtrajectory was separately computed. MSD fitting with a simple Brownian motion model results in a D value for each types of region, D_{in} and D_{out}. However, this analysis has several drawbacks: (i) it assumes that the boundaries of these regions (along the trajectory) can be easily identified and (ii) the MSD analysis does not permit an accurate determination of the type of diffusion, and hence the corresponding diffusion constant. At least qualitatively, MSD analysis reveals that diffusion in GM1-rich domains is much slower than that outside them ($D_{\text{in}} << D_{\text{out}}$ in Figure S5). To obtain a quantitative measure, we perform a PDSD analysis on the same trajectory. In general, the number of diffusion regimes identified in this manner corresponds to that obtained using the more subjective MSD approach (Figure S5) and provide accurate diffusion coefficients. When combining subtrajectories MSD analysis, instantaneous diffusion analysis and PDSD analysis of the same trajectory, it is then straightforward to assign an accurate D value to regions and/or time periods exhibiting the slowest diffusion (D_{in}) or the fastest diffusion (D_{out}).

Acknowledgments

The authors would like to thank Ms. Millie Gentry for help with the avidin-CD14 construct and Mr. Peter Masatani and Mr. Jonathan Chuang for their

assistance with isolation of detergent resistant membranes. We also thank Ron Lin and Sri Prasad for help with data analysis and Esther Richler for help with confocal imaging. The authors would also like to thank two anonymous reviewers for their thorough analysis and helpful suggestions to improve former versions of our manuscript. Confocal fluorescent microscopy was performed at the UCLA/CNSI Advanced Light Microscopy Shared Facility. This work was supported by NIH/NIBIB BRP grant 5-R01-EB000312 and the NSF, The Center for Biophotonics, an NSF Science and Technology Center managed by the University of California, Davis, under Cooperative Agreement PHY0120999.

Supporting Information

Additional Supporting Information may be found in the online version of this article:

Supporting Material and Methods

Supporting Discussion

Figure S1: Confocal fluorescence recovery after photobleaching (FRAP) of Av-GPI in the plasma membrane of HeLa cells. A) Sequence of images illustrating the fluorescence recovery after photobleaching in a 5 μm radius circular ROI in the ventral membrane of a HeLa cell. Scale bar: 5 μm. B) Averaged fluorescence recovery curves for several HeLa cells bleached in a 3 μm radius ROI at 37°C (circle, $n = 19$) or at room temperature (RT, diamond, $n = 17$). Standard deviations for each data point were omitted for clarity but considered for the fit. Faster fluorescence recovery for smaller, 1.5 μm radius bleached spots (result not shown) indicated that the recovery was dominated by diffusion. The apparent diffusion coefficient (D) and the immobile fraction were thus derived by non-linear least square fit of the recovery curves to the lateral diffusion equations for uniform circular bleach spots. For both temperatures, the FRAP recovery curves were better described with a two-component lateral diffusion model (37°C, blue, F-test $p < 0.0001$; and RT, red, F-test $p < 0.0001$) than with a one-component model. At 37°C $79 \pm 12\%$ of Av-GPI appear to diffuse with $D_{\text{fast}}^{\text{FRAP/37}c} = 1.7 \pm 0.310^{-1}$ μm^2/ s while $16 \pm 8\%$ of Av-GPI diffuse with a diffusion coefficient about 20 times smaller ($D_{\text{slow}}^{\text{FRAP/37}c} = 7.96 \pm 0.06 \times 10^{-3}$ μm^2/ s) and $5 \pm 4\%$ of GPI-test probes were found to be immobile. The apparent diffusion coefficient of both fast and slow population were reduced about three-fold when FRAP measurements were performed at RT (~ 27°C). At RT, $81 \pm 12\%$ of Av-GPI diffused with $D_{\text{fast}}^{\text{FRAP/RT}} = 6.5 \pm 1.9 \times 10^{-2}$ μm2/s and $15 \pm 7\%$ diffused with $D_{\text{slow}}^{\text{FRAP/RT}} = 2.66 \pm 0.02 \times 10^{-3}$ μm2/s. The fraction of immobile Av-GPI ($4 \pm 5\%$) remained unchanged. SD, standard deviation.

Figure S2: Analysis of the oligomeric state of Av-GPI in the membrane of HeLa cells. A) Parallel Western blot analysis of native chicken avidin (right) and Av-GPI (left) extracted from the plasma membrane of HeLa cells and run on 15% SDS-PAGE. The blot shows that native avidin prepared in SDS buffer without boiling migrate as a mixture of high molecular weight species (lane 5). Upon boiling, the high molecular band disappeared and was replaced by a ~17 kDa band corresponding to monomeric avidin (lane 7). As previously reported, the addition of biotin before boiling significantly enhanced the recovery of high molecular weight complexes (lane 8). A different behavior was observed for Av-GPI. In samples that were not boiled, the chimeric protein migrated as a homogenous high molecular weight complex with the predicted size for a ~ 120 kDa tetramer (lanes 1 and 2). Upon boiling, as observed for avidin, the biotin-free complex was converted to a ~ 30 kDa monomer (lane 3). This value is slightly above the theoretical molecular weight for the non-glycosylated and monomeric form of Av-GPI (~ 23 kDa) and may indicate the presence of glycosylated moieties. The addition of biotin resulted in the predominant recovery of the tetramers (lane 4). B) Western blot analysis of Av-GPI extracted from the plasma membrane of HeLa cells after *in situ* acetylation with NHS-acetate and run on a 4–20% SDS-PAGE. Under non-denaturing conditions (no boiling), acetylated Av-GPI migrated essentially as ~ 120 kDa band as expected for the tetrameric form of Av-GPI (lane 2). No obvious enrichment in multi-tetramers, trimers, dimers, or monomers of Av-GPI were observed, confirming that Av-GPI form stable tetramers in the membrane of HeLa cells. A boiled sample of acetylated Av-GPI (lane 3) was used as a control and compared to Av-GPI from membrane preparation not treated with NHS-acetate (lane 1). Both samples migrated between 20–30 kDa as expected for Av-GPI monomers (~23 kDa). These results indicate that Av-GPI does not appear to form multi-oligomers compared to native avidin and most likely exists as a glycosylated homotetramer attached to the membrane.

Figure S3: Av-GPI labeled with quasi-monovalent or multivalent biotinylated qdots have similar diffusive behaviors. A) Gel shift assay in 1% agarose to evaluate the binding properties of quasi-monovalent or multivalent qdots to Neutravidin at increasing concentrations of Neutravidin (10 000, 5000, 2500, 1250, 625, 312, 156, 78, 39, 19.5, 9.75, 5 nM). Qdot fluorescence was detected on a fluorescence gel scanner. * indicates no Neutravidin. B) Distribution of diffusion coefficients after single-qdot tracking of Av-GPI labeled with quasi-monovalent (top) or multivalent (bottom) biotinylated qdots in live HeLa cells. C) Examples of Av-GPI trajectories for quasi-monovalent (top) or multivalent qdots (bottom).

Figure S4: Single-dye tracking of Av-GPI with monovalent Alexa 488 biocytin at room temperature. A) Example of Av-GPI trajectories after tracking with monovalent Alexa 488 biocytin. B) MSD plots for 81 Av-GPI labeled with Alexa 488 biocytin (blue curves) and ensemble MSD plot obtained by pooling together the square displacements of all trajectories (red curve). C) Example of Av-GPI trajectory with two diffusion coefficients. The squared trajectory in (A) was sufficiently long (4.6 s) to detect a change in diffusion when plotting the instantaneous diffusion coefficient over time. D) Global PDSD analysis of the same 81 Av-GPI traces in (B). The PDSD curves were fitted with three fitting exponents for comparison with a similar global PDSD analysis of qdots labeled Av-GPI traces (data can be viewed at http://fpinaud.bol.ucla.edu/index_files/Traffic.htm). The three $r_i^2 t$ curves recovered were well fitted with a normal diffusion model $< r^2 >= 4Dt$ with $D_1 = 1.4 \times 10^{-1}$ μm^2/ s (18%), $D_2 = 4.0 \times 10^{-2}$ μm^2/ s (54%) and $D_3 = 5.7 \times 10^{-3}$ μm^2/ s (28%), for $r_1^2(t)$, $r_2^2(t)$ and $r_3^2(t)$, respectively.

Figure S5: Example study of Av-GPI colocalization with GM1-rich domains by MSD analysis of subtrajectories and PDSD analysis together with PDSD analysis of Monte Carlo simulated trajectories. A) The trajectory of a tracked Av-GPI is overlaid with the green CTxB mean intensity projection image. Scale bar 500 nm. B) Colocalization of Av-GPI with a GM1-rich domain is confirmed by studying qdot (red) and CTxB signal (green) along the GPI-test probe trajectory. Periods during which signals are above background (gray) and overlap are selected (ROI). C) The sub-trajectory corresponding to the selected temporal ROI is automatically highlighted. D) MSD are then computed for the full trajectory (black), the selected ROI and colocalizing sub-trajectory (green) or the non colocalizing sub-trajectory (blue). MSD are then fitted over 10% with a simple Brownian diffusion model (red). The fit curve of the full trajectory MSD has been omitted for clarity. E) Diffusion coefficients are determined from fits of 10% of the MSD in (D). For this particular Av-GPI molecule, the diffusion coefficient within the GM1-rich domain is ~ 30 times smaller than it is outside the domain. F) PDSD analysis on the same trajectory is then performed for consistency and to verify the diffusion values determined from sub-trajectory MSDs. The diffusion coefficients fall within the fast and slow sub-populations of the diffusion histograms (Figure 3B). G) PDSD analysis of Monte Carlo simulated trajectories. (i) A simulated trajectory undergoing a change in diffusion mode from free diffusion (D_1) to restricted diffusion (D_2) into

a circular domain of radius $R = 100$ nm. The diffusion constants chosen in this simulation correspond to the modal values of the fast and slow diffusion regimes reported in the text. Uncertainty in position determination was set to 30 nm, a typical value observed in our experiments. The particle was located in the slow domain for 60% of the trajectory duration (100 s). (ii) PDSD analysis of the trace in (i) over 3% of the time lags. (iii) Fit of PDSD in (ii) results in two $r_i^2(t)$ curves (open circles). $r_1^2(t)$ could be fitted with a simple diffusion mode (black curve) resulting in a measured diffusion coefficient $D_{1,\mathrm{mes}} \cdot r_2^2(t)$ (red circles) was fitted with a restricted diffusion model (red curve) and yielded $D_{2,\mathrm{mes}}$ and R in good agreement with the input values of the simulation. The reported uncertainty value is that associated with the restricted diffusion regime. The computed uncertainty associated with the simple diffusion regime is 58 nm. Notice that the graph is represented in logarithmic scale because of the large difference in D values.

Figure S6: Correlation of colocalization and diffusion coefficients of Av-GPI and caveolae. Three examples of simultaneous caveolae and Av-GPI tracking. Trajectories in (A) and (B) correspond to images of Figure 6E. The trajectory in (C) corresponds to one image of Figure 6C. Diffusion coefficients were obtained by PDSD analysis as illustrated on the right. In (A) and (B), Av-GPI and caveola colocalize within the experimental uncertainty of the overlay of the green and red channel (~1 pixel). The diffusion coefficients are reasonably close and suggest trapping of Av-GPI in the caveolar pit. In (C) the GPI-test probe switches diffusion regimen in close proximity to a caveola.

Figure S7: Quantification of membrane cholesterol by filipin staining of Av-GPI expressing cells. A) Confocal imaging of filipin in control cells, cells treated with 10 μM lovastatin for 30 h or cells treated with 10 mM mβCD for 1 h. Acute cholesterol depletion with mβCD removes most of the membrane cholesterol and poor filipin staining is observed. Scale bar: 10 μm. B) Quantification of membrane cholesterol from filipin fluorescence intensity. Lovastatin treatment did not result in a significant decrease in membrane cholesterol compared to control cells (86% ±22%, $n = 47$). After treatment with mβCD, however, the cholesterol content in cell membranes is strongly reduced (17 ± 7%, $n = 34$).

Figure S8: Effect of cholesterol depletion on the actin cytoskeleton and the distribution of GM1 in fixed HeLa cells expressing Av-GPI. A) The organization of the actin cytoskeleton is impacted by cholesterol depleting drugs. Acute reduction in membrane cholesterol with 10 mM mβCD treatment for 1 h leads to a slight rounding up of adherent HeLa cells and reduced cell contacts. Although some stress fibers are present, they appear less defined than in untreated cells and actin-rich foci and microspikes are visible. Cholesterol depletion with 10 μM lovastatin for 30 h led to less abundant and less defined stress fibers. The cortical actin network lining the inner surface of the plasma membrane is also irregular and cell contacts are reduced. B) The membrane distribution of GM1 is affected by cholesterol depleting drugs. While GM1 are distributed homogeneously in the plasma membrane of untreated cells, acute cholesterol depletion by mβCD redirects GM1 to perinuclear compartments (arrows) and significantly decreases GM1 membrane content. Milder cholesterol depletion with lovastatin does not strongly affect the distribution of GM1 in the membrane. Only limited perinuclear localization of GM1 is observed (arrows). Inserts: DIC images of micrographs. Scale bars: 20 μm.

Figure S9: Cholesterol depletion with lovastatin has little effect on the diffusion of Av-GPI. A) Confocal fluorescence image of Av-GPI in the plasma membrane of HeLa cells after 30 h cholesterol depletion with 10 μM lovastatin. Insert: DIC image. Scale bar: 20 μm. B) Distribution of Av-GPI diffusion coefficients for lovastatin treated cells in the presence of the Alexa 488 labeled CTxB. The two populations of fast and slow Av-GPI have diffusion coefficients similar to untreated cells with $\hat{D}_{\mathrm{fast}}^{\mathrm{lova/+CT\times B}} = 2.8 \times 10^{-2}\ \mu m^2/s$ (SE: $2.0–4.0 \times 10^{-2}\ \mu m^2/s$, 51%) and $\hat{D}_{\mathrm{slow}}^{\mathrm{lova/+CT\times B}} = 1.0 \times 10^{-4}\ \mu m^2/s$ (SE: $0.8–1.4 \times 10^{-4}\ \mu m^2/s$, 36%). Only 7% of all Av-GPI repartitioned between the fast and slow populations during tracking. C) CTxB $\sum I_{\mathrm{mean}}$ image of an ROI of the plasma membrane for a cell treated with lovastatin. Av-GPI trajectories are overlaid on the image. As observed for untreated cells stained with CTxB, about 65% of slow Av-GPI were colocalized with GM1-rich CTxB-labeled domains, while faster Av-GPI diffuse around these structures. Scale bar: 1 μm. D) Modes of diffusion for Av-GPI after lovastatin treatment. The diffusion modes of fast and slow Av-GPI are not significantly influenced by lovastatin, and are similar to those of untreated cells.

Figure S10: Effects of actin cytoskeleton disruption on membrane organization and diffusion of Av-GPI and GM1 in HeLa cells. Cells were incubated with 10 μM latrunculin-A for 45 min at the end of the serum-starving period and prepared for imaging as described in *Materials and Methods*. Latrunculin-A was kept in the cell medium at all steps including imaging. A) F-actin staining after treatment with latrunculin-A, fixation and permeabilization of HeLa cells. The actin cytoskeleton was completely disrupted. Membrane retraction and changes in cell shape are clearly visible (DIC image). Scale bar 20 μm. B) Confocal fluorescence image of the distribution of Av-GPI and GM1 upon disruption of cortical actin. Both GPI-test probes and GM1 were located in bright, large and co-localizing membrane patches bound to the coverslip (arrows) or distributed on the cell membrane. C) Distribution of Av-GPI diffusion coefficients for latrunculin-A treated cells in the presence of Alexa-488 CTxB. Only GPI-test probes that diffused clearly and did not change diffusion regime during the tracking were analyzed. The modal diffusion coefficient was $\hat{D}_{\mathrm{fast}}^{\mathrm{lat\text{-}A}} = 1.6 \times 10^{-1}\ \mu m^2/s$ (SE: $1.4–2.1 \times 10^{-1}\ \mu m^2/s$). D) Examples of Av-GPI trajectories in latrunculin-A treated cells.

Table S1: Distributions and quantification of Av-GPI and transferrin receptor in flotation gradients.

Table S2: Diffusion models.

Table S3: Diffusion coefficients of Av-GPI measured with various techniques and under different conditions.

Video 1: Imaging of qdot-labeled Av-GPI in the ventral membrane of HeLa cells (just before addition of CTxB) by TIRF microscopy. The typical on/off behavior of single qdots is observed. Some qdots freely diffusing in solution (between the coverslip and the membrane) can be seen binding to Av-GPI. These events are characterized by a sudden change from a very fast diffusion in three-dimension to a slower diffusion in two-dimension, in the plane of the plasma membrane. Acquisition: 100 ms/frame; Display: 30 ms/frame.

Video 2: Diffusion of Alexa 488 biocytin-labeled Av-GPI. Acquisition: 60 ms/frame; Display: 30 ms/frame.

Video 3: Dual-color TIRF imaging of qdot-labeled Av-GPI (red) and Alexa-488 CTxB labeled GM1 glycosphingolipids (green). Notice that the contrast of the point-spread-function of qdots was intentionally increased to facilitate visualization. Acquisition: 100 ms/frame; Display: 30 ms/frame.

Video 4: Example of qdot-labeled Av-GPI (red) diffusing either in stationary GM1-rich microdomains (green), outside these domains or partitioning in and out of the domains. The qdot channel was overlaid on the mean intensity projection image of the Alexa-488 CTxB-labeled GM1 channel. The contrast of the point-spread-function of qdots was intentionally increased to facilitate visualization. Acquisition: 100 ms/frame; Display: 30 ms/frame.

Video 5: Example of the entry and slowing down of a qdot-labeled Av-GPI (red) in a stationary GM1-rich domain (green). The qdot channel was

overlaid on the mean intensity projection image of the Alexa-488 CTxB-labeled GM1 channel. Acquisition: 100 ms/frame; Display: 30 ms/frame.

Video 6: Example of exit and increased diffusion of a qdot-labeled Av-GPI (red) out of a stationary GM1-rich domain (green). The qdot channel was overlaid on the mean intensity projection image of the Alexa-488 CTxB-labeled GM1 channel. Acquisition: 100 ms/frame; Display: 30 ms/frame.

Video 7: Dual-color TIRF imaging of qdot-labeled Av-GPI (red) and Caveolin-1-EGFP labeled caveolae (green). Acquisition: 100 ms/frame; Display: 30 ms/frame.

Video 8: Dual-color TIRF imaging of qdot-labeled Av-GPI (red) and Alexa-488 CTxB-labeled GM1 (green) after treatment with lovastatin (10 μM). Acquisition: 100 ms/frame; Display: 30 ms/frame.

Video 9: Dual-color TIRF imaging of qdot-labeled Av-GPI (red) and Alexa-488 CTxB-labeled GM1 (green) after treatment with mβCD (10 mM). Acquisition: 100 ms/frame; Display: 30 ms/frame.

Video 10: Dual-color TIRF imaging of qdot-labeled Av-GPI (red) and Alexa-488 CTxB cholera toxin B-labeled GM1 (green) after treatment with latrunculin-A (10 μM). Acquisition: 100 ms/frame; Display: 30 ms/frame.

Please note: Wiley-Blackwell are not responsible for the content or functionality of any supporting materials supplied by the authors. Any queries (other than missing material) should be directed to the corresponding author for the article.

References

1. Singer S, Nicolson G. The fluid mosaic model of the structure of cell membranes cell membranes are viewed as 2 dimensional solutions of oriented globular proteins and lipids. Science 1972;175:720–731.
2. Ryan TA, Myers J, Holowka D, Baird B, Webb WW. Molecular crowding on the cell surface. Science 1988;239:61–64.
3. Edidin M. The state of lipid rafts: from model membranes to cells. Annu Rev Biophys Biomol Struct 2003;32:257–283.
4. Simons K, Vaz WLC. Model systems, lipid rafts, and cell membranes. Annu Rev Biophys Biomol Struct 2004;33:269–295.
5. Kusumi A, Koyama-Honda I, Suzuki K. Molecular dynamics and interactions for creation of stimulation-induced stabilized rafts from small unstable steady-state rafts. Traffic 2004;5:213–230.
6. Jacobson K, Mouritsen OG, Anderson RGW. Lipid rafts: at a crossroad between cell biology and physics. Nat Cell Biol 2007;9:7–14.
7. Kusumi A, Sako Y, Yamamoto M. Confined lateral diffusion of membrane receptors as studied by single particle tracking (nanovid microscopy). Effects of calcium-induced differentiation in cultured epithelial cells. Biophys J 1993;65:2021–2040.
8. Kusumi A, Nakada C, Ritchie K, Murase K, Suzuki K, Murakoshi H, Kasai RS, Kondo J, Fujiwara T. Paradigm shift of the plasma membrane concept from the two-dimensional continuum fluid to the partitioned fluid: High-speed single-molecule tracking of membrane molecules. Annu Rev Biophys Biomol Struct 2005;34:351–378.
9. Douglass AD, Vale RD. Single-molecule microscopy reveals plasma membrane microdomains created by protein-protein networks that exclude or trap signaling molecules in T cells. Cell 2005;121:937–950.
10. Simons K, van Meer G. Lipid sorting in epithelial-cells. Biochemistry 1988;27:6197–6202.
11. Simons K, Ikonen E. Functional rafts in cell membranes. Nature 1997;387:569–572.
12. Leyton L, Quest AFG. Introduction to supramolecular complex formation in cell signaling and disease. Biol Res 2002;35:117–125.
13. Simons K, Toomre D. Lipid rafts and signal transduction. Nat Rev Mol Cell Biol 2000;1:31–39.
14. Pike LJ. Lipid rafts: bringing order to chaos. J Lipid Res 2003;44:655–667.
15. Schroeder R, London E, Brown D. Interactions between saturated acyl chains confer detergent resistance on lipids and glycosylphosphatidylinositol (GPI)-anchored proteins - GPI-anchored proteins in liposomes and cells show similar behavior. Proc Natl Acad Sci U S A 1994;91:12130–12134.
16. Benting J, Rietveld A, Ansorge I, Simons K. Acyl and alkyl chain length of GPI-anchors is critical for raft association in vitro. FEBS Lett 1999;462:47–50.
17. Dietrich C, Bagatolli LA, Volovyk ZN, Thompson NL, Levi M, Jacobson K, Gratton E. Lipid rafts reconstituted in model membranes. Biophys J 2001;80:1417–1428.
18. Veatch SL, Keller SL. Organization in lipid membranes containing cholesterol. Phys Rev Lett 2002;89:268101.
19. Milhiet PE, Giocondi MC, Baghdadi O, Ronzon F, Roux B, Le Grimellec C. Spontaneous insertion and partitioning of alkaline phosphatase into model lipid rafts. EMBO Rep 2002;3:485–490.
20. Baumgart T, Hess ST, Webb WW. Imaging coexisting fluid domains in biomembrane models coupling curvature and line tension. Nature 2003;425:821–824.
21. Brown DA, Rose JK. Sorting of Gpi-anchored proteins to glycolipid-enriched membrane subdomains during transport to the apical cell-surface. Cell 1992;68:533–544.
22. Gaus K, Gratton E, Kable EPW, Jones AS, Gelissen I, Kritharides L, Jessup W. Visualizing lipid structure and raft domains in living cells with two-photon microscopy. Proc Natl Acad Sci U S A 2003;100:15554–15559.
23. Gallegos AM, Storey SM, Kier AB, Schroeder F, Ball JM. Structure and cholesterol dynamics of caveolae/raft and nonraft plasma membrane domains. Biochemistry 2006;45:12100–12116.
24. Anderson RGW, Jacobson K. Cell biology - A role for lipid shells in targeting proteins to caveolae, rafts, and other lipid domains. Science 2002;296:1821–1825.
25. Pike LJ. Rafts defined: a report on the Keystone Symposium on lipid rafts and cell function. J Lipid Res 2006;47:1597–1598.
26. Lagerholm BC, Weinreb GE, Jacobson K, Thompson NL. Detecting microdomains in intact cell membranes. Annu Rev Phys Chem 2005;56:309–336.
27. Michalet X, Weiss S. Single-molecule spectroscopy and microscopy. C R Phys 2002;3:619–644.
28. Wiseman PW, Brown CM, Webb DJ, Hebert B, Johnson NL, Squier JA, Ellisman MH, Horwitz AF. Spatial mapping of integrin interactions and dynamics during cell migration by Image Correlation Microscopy. J Cell Sci 2004;117:5521–5534.
29. Bacia K, Scherfeld D, Kahya N, Schwille P. Fluorescence correlation spectroscopy relates rafts in model and native membranes. Biophys J 2004;87:1034–1043.
30. Lenne PF, Wawrezinieck L, Conchonaud F, Wurtz O, Boned A, Guo XJ, Rigneault H, He HT, Marguet D. Dynamic molecular confinement in the plasma membrane by microdomains and the cytoskeleton meshwork. EMBO J 2006;25:3245–3256.
31. Rao M, Mayor S. Use of Forster's resonance energy transfer microscopy to study lipid rafts. Biochim Biophys Acta 2005;1746:221–233.
32. Schütz GJ, Kada G, Pastushenko VP, Schindler H. Properties of lipid microdomains in a muscle cell membrane visualized by single molecule microscopy. EMBO J 2000;19:892–901.
33. Saxton MJ, Jacobson K. Single-particle tracking: applications to membrane dynamics. Annu Rev Biophys Biomol Struct 1997;26:373–399.

34. Daumas F, Destainville N, Millot C, Lopez A, Dean D, Salome L. Confined diffusion without fences of a G-protein-coupled receptor as revealed by single particle tracking. Biophys J 2003;84:356–366.
35. Ritchie K, Shan XY, Kondo J, Iwasawa K, Fujiwara T, Kusumi A. Detection of non-Brownian diffusion in the cell membrane in single molecule tracking. Biophys J 2005;88:2266–2277.
36. Lasne D, Blab GA, Berciaud S, Heine M, Groc L, Choquet D, Cognet L, Lounis B. Single nanoparticle photothermal tracking (SNaPT) of 5-nm gold beads in live cells. Biophys J 2006;91:4598–4604.
37. Michalet X, Pinaud FF, Bentolila LA, Tsay JM, Doose S, Li JJ, Sundaresan G, Wu AM, Gambhir SS, Weiss S. Quantum dots for live cells, in vivo imaging, and diagnostics. Science 2005;307:538–544.
38. Dahan M, Levi S, Luccardini C, Rostaing P, Riveau B, Triller A. Diffusion dynamics of glycine receptors revealed by single-quantum dot tracking. Science 2003;302:442–445.
39. Groc L, Heine M, Cognet L, Brickley K, Stephenson FA, Lounis B, Choquet D. Differential activity-dependent regulation of the lateral mobilities of AMPA and NMDA receptors. Nat Neurosci 2004;7:695–696.
40. Chen HF, Titushkin I, Stroscio M, Cho M. Altered membrane dynamics of quantum dot-conjugated integrins during osteogenic differentiation of human bone marrow derived progenitor cells. Biophys J 2007;92:1399–1408.
41. Bates IR, Hebert B, Luo YS, Liao J, Bachir AI, Kolin DL, Wiseman PW, Hanrahan JW. Membrane lateral diffusion and capture of CFTR within transient confinement zones. Biophys J 2006;91:1046–1058.
42. Haggie PM, Kim JK, Lukacs GL, Verkman AS. Tracking of quantum dot-labeled CFTR shows near immobilization by C-terminal PDZ interactions. Mol Biol Cell 2006;17:4937–4945.
43. Pinaud F, King D, Moore HP, Weiss S. Bioactivation and cell targeting of semiconductor CdSe/ZnS nanocrystals with phytochelatin-related peptides. J Am Chem Soc 2004;126:6115–6123.
44. Simmons DL, Tan S, Tenen DG, Nicholsonweller A, Seed B. Monocyte antigen Cd14 is a phospholipid anchored membrane-protein. Blood 1989;73:284–289.
45. Pugin J, Kravchenko VV, Lee JD, Kline L, Ulevitch RJ, Tobias PS. Cell activation mediated by glycosylphosphatidylinositol-anchored or transmembrane forms of CD14. Infect Immun 1998;66:1174–1180.
46. Poussin C, Foti M, Carpentier JL, Pugin J. CD14-dependent endotoxin internalization via a macropinocytic pathway. J Biol Chem 1998;273:20285–20291.
47. Green NM. Avidin and streptavidin. Methods Enzymol 1990;184:51–67.
48. Lehtolainen P, Wirth T, Taskinen AK, Lehenkari P, Leppanen O, Lappalainen M, Pulkkanen K, Marttila A, Marjomaki V, Airenne KJ, Horton M, Kulomaa MS, Yla-Herttuala S. Targeting of biotinylated compounds to its target tissue using a low-density lipoprotein receptor-avidin fusion protein. Gene Ther 2003;10:2090–2097.
49. Hanada K, Nishijima M, Akamatsu Y, Pagano RE. Both sphingolipids and cholesterol participate in the detergent insolubility of alkaline-phosphatase, a glycosylphosphatidylinositol-anchored protein, in mammalian membranes. J Biol Chem 1995;270:6254–6260.
50. Harder T, Scheiffele P, Verkade P, Simons K. Lipid domain structure of the plasma membrane revealed by patching of membrane components. J Cell Biol 1998;141:929–942.
51. Reig N, van der Goot FG. About lipids and toxins. FEBS Lett 2006;580:5572–5579.
52. Lacoste TD, Michalet X, Pinaud F, Chemla DS, Alivisatos AP, Weiss S. Ultrahigh-resolution multicolor colocalization of single fluorescent probes. Proc Natl Acad Sci U S A 2000;97:9461–9466.
53. Michalet X, Lacoste TD, Weiss S. Ultrahigh-resolution colocalization of spectrally resolvable point-like fluorescent probes. Methods 2001;25:87–102.
54. Shimizu KT, Neuhauser RG, Leatherdale CA, Empedocles SA, Woo WK, Bawendi MG. Blinking statistics in single semiconductor nanocrystal quantum dots. Phys Rev B 2001;63:205316.
55. Schütz GJ, Schindler H, Schmidt T. Single-molecule microscopy on model membranes reveals anomalous diffusion. Biophys J 1997;73:1073–1080.
56. Schmidt K, Nichols BJ. A barrier to lateral diffusion in the cleavage furrow of dividing mammalian cells. Curr Biol 2004;14:1002–1006.
57. Rothberg KG, Heuser JE, Donzell WC, Ying YS, Glenney JR, Anderson RGW. Caveolin, a protein-component of caveolae membrane coats. Cell 1992;68:673–682.
58. Kurzchalia TV, Parton RG. Membrane microdomains and caveolae. Curr Opin Cell Biol 1999;11:424–431.
59. Schnitzer JE, McIntosh DP, Dvorak AM, Liu J, Oh P. Separation of caveolae from associated microdomains of Gpi-anchored proteins. Science 1995;269:1435–1439.
60. Cheng ZJ, Singh RD, Marks DL, Pagano RE. Membrane microdomains, caveolae, and caveolar endocytosis of sphingolipids (Review. Mol Membr Biol 2006;23:101–110.
61. Parton RG. Ultrastructural-localization of gangliosides - Gm(1) is concentrated in caveolae. J Histochem Cytochem 1994;42:155–166.
62. Orlandi PA, Fishman PH. Filipin-dependent inhibition of cholera toxin: evidence for toxin internalization and activation through caveolae-like domains. J Cell Biol 1998;141:905–915.
63. Thomsen P, Roepstorff K, Stahlhut M, van Deurs B. Caveolae are highly immobile plasma membrane microdomains, which are not involved in constitutive endocytic trafficking. Mol Biol Cell 2002;13:238–250.
64. Tagawa A, Mezzacasa A, Hayer A, Longatti A, Pelkmans L, Helenius A. Assembly and trafficking of caveolar domains in the cell: caveolae as stable, cargo-triggered, vesicular transporters. J Cell Biol 2005;170:769–779.
65. Kahya N, Scherfeld D, Bacia K, Poolman B, Schwille P. Probing lipid mobility of raft-exhibiting model membranes by fluorescence correlation spectroscopy. J Biol Chem 2003;278:28109–28115.
66. Ilangumaran S, Hoessli DC. Effects of cholesterol depletion by cyclodextrin on the sphingolipid microdomains of the plasma membrane. Biochem J 1998;335:433–440.
67. Bifulco M, Laezza C, Aloi SM, Garbi C. Mevalonate controls cytoskeleton organization and cell morphology in thyroid epithelial-cells. J Cell Physiol 1993;155:340–348.
68. Essig M, Nguyen G, Prie D, Escoubet B, Sraer JD, Friedlander G. 3-hydroxy-3-methylglutaryl coenzyme A reductase inhibitors increase fibrinolytic activity in rat aortic endothelial cells - Role of geranylgeranylation and Rho proteins. Circ Res 1998;83:683–690.
69. Pagano RE, Puri V, Dominguez M, Marks DL. Membrane traffic in sphingolipid storage diseases. Traffic 2000;1:807–815.
70. Hao MM, Mukherjee S, Maxfield FR. Cholesterol depletion induces large scale domain segregation in living cell membranes. Proc Natl Acad Sci U S A 2001;98:13072–13077.
71. Sackmann E. Thermo-elasticity and adhesion as regulators of cell membrane architecture and function. J Phys Condens Matter 2006;18:R785–R825.
72. Rodgers W, Farris D, Mishra S. Merging complexes: properties of membrane raft assembly during lymphocyte signaling. Trends Immunol 2005;26:97–103.
73. Holowka D, Gosse JA, Hammond AT, Han XM, Sengupta P, Smith NL, Wagenknecht-Wiesner A, Wu M, Young RM, Baird B. Lipid segregation and IgE receptor signaling: a decade of progress. Bba-Mol Cell Res 2005;1746:252–259.
74. Coue M, Brenner SL, Spector I, Korn ED. Inhibition of actin polymerization by latrunculin-A. FEBS Lett 1987;213:316–318.
75. Laitinen OH, Nordlund HR, Hytonen VP, Uotila STH, Marttila AT, Savolainen J, Airenne KJ, Livnah O, Bayer EA, Wilchek M, Kulomaa MS. Rational design of an active avidin monomer. J Biol Chem 2003;278:4010–4014.

76. Laitinen OH, Airenne KJ, Marttila AT, Kulik T, Porkka E, Bayer EA, Wilchek M, Kulomaa MS. Mutation of a critical tryptophan to lysine in avidin or streptavidin may explain why sea urchin fibropellin adopts an avidin-like domain. FEBS Lett 1999;461:52–58.
77. Gambin Y, Lopez-Esparza R, Reffay M, Sierecki E, Gov NS, Genest M, Hodges RS, Urbach W. Lateral mobility of proteins in liquid membranes revisited. Proc Natl Acad Sci U S A 2006;103:2098–2102.
78. Chen Y, Yang B, Jacobson K. Transient confinement zones: a type of lipid raft?. Lipids 2004;39:1115–1119.
79. Murase K, Fujiwara T, Umemura Y, Suzuki K, Iino R, Yamashita H, Saito M, Murakoshi H, Ritchie K, Kusumi A. Ultrafine membrane compartments for molecular diffusion as revealed by single molecule techniques. Biophys J 2004;86:4075–4093.
80. Suzuki KGN, Fujiwara TK, Sanematsu F, Iino R, Edidin M, Kusumi A. GPI-anchored receptor clusters transiently recruit Lyn and G alpha for temporary cluster immobilization and Lyn activation: single-molecule tracking study 1. J Cell Biol 2007;177:717–730.
81. Chen Y, Thelin WR, Yang B, Milgram SL, Jacobson K. Transient anchorage of cross-linked glycosyl-phosphatidylinositol-anchored proteins depends on cholesterol, Src family kinases, caveolin, and phosphoinositides. J Cell Biol 2006;175:169–178.
82. Hicks BW, Angelides KJ. Tracking movements of lipids and Thy1 molecules in the plasmalemma of living fibroblasts by fluorescence video microscopy with nanometer-scale precision. J Membr Biol 1995;144:231–244.
83. Sheets ED, Lee GM, Simson R, Jacobson K. Transient confinement of a glycosylphosphatidylinositol-anchored protein in the plasma membrane. Biochemistry 1997;36:12449–12458.
84. Simson R, Yang B, Moore SE, Doherty P, Walsh FS, Jacobson KA. Structural mosaicism on the submicron scale in the plasma membrane. Biophys J 1998;74:297–308.
85. Vrljic M, Nishimura SY, Brasselet S, Moerner WE, McConnell HM. Translational diffusion of individual class II MHC membrane proteins in cells. Biophys J 2002;83:2681–2692.
86. Kenworthy AK, Nichols BJ, Remmert CL, Hendrix GM, Kumar M, Zimmerberg J, Lippincott-Schwartz J. Dynamics of putative raft-associated proteins at the cell surface. J Cell Biol 2004;165:735–746.
87. Nichols BJ. GM1-containing lipid rafts are depleted within clathrin-coated pits. Curr Biol 2003;13:686–690.
88. Fujita A, Cheng JL, Hirakawa M, Furukawa K, Kusunoki S, Fujimoto T. Gangliosides GM1 and GM3 in the living cell membrane form clusters susceptible to cholesterol depletion and chilling. Mol Biol Cell 2007;18:2112–2122.
89. Lingwood D, Ries J, Schwille P, Simons K. Plasma membranes are poised for activation of raft phase coalescence at physiological temperature. Proc Natl Acad Sci U S A 2008;105:10005–10010.
90. Sharma P, Varma R, Sarasij RC, Ira, Gousset K, Krishnamoorthy G, Rao M, Mayor S. Nanoscale organization of multiple GPI-anchored proteins in living cell membranes. Cell 2004;116:577–589.
91. Scalettar BA, Abney JR. Molecular crowding and protein diffusion in biological membranes. Comm Mol Cell Biophys 1991;7:79–107.
92. Nicolau DV, Burrage K, Parton RG, Hancock JF. Identifying optimal lipid raft characteristics required to promote nanoscale protein-protein interactions on the plasma membrane. Mol Cell Biol 2006;26:313–323.
93. Mayor S, Rothberg KG, Maxfield FR. Sequestration of Gpi-anchored proteins in caveolae triggered by cross-linking. Science 1994;264:1948–1951.
94. Fujimoto T. GPI-anchored proteins, glycosphingolipids, and sphingomyelin are sequestered to caveolae only after crosslinking. J Histochem Cytochem 1996;44:929–941.
95. Parton RG, Simons K. The multiple faces of caveolae. Nat Rev Mol Cell Biol 2007;8:185–194.
96. Wu M, Fan J, Gunning W, Ratnam M. Clustering of GPI-anchored folate receptor independent of both cross-linking and association with caveolin. J Membr Biol 1997;159:137–147.
97. Montesano R. Inhomogeneous distribution of filipin-sterol complexes in smooth-muscle cell plasma-membrane. Nature 1979;280:328–329.
98. Makiya R, Thornell LE, Stigbrand T. Placental alkaline-phosphatase, a Gpi-anchored protein, is clustered in clathrin-coated vesicles. Biochem Biophys Res Commun 1992;183:803–808.
99. Kitchens RL, Wang PY, Munford RS. Bacterial lipopolysaccharide can enter monocytes via two CD14-dependent pathways. J Immunol 1998;161:5534–5545.
100. Torgersen ML, Skretting G, van Deurs B, Sandvig K. Internalization of cholera toxin by different endocytic mechanisms. J Cell Sci 2001;114:3737–3747.
101. Kirkham M, Fujita A, Chadda R, Nixon SJ, Kurzchalia TV, Sharma DK, Pagano RE, Hancock JF, Mayor S, Parton RG. Ultrastructural identification of uncoated caveolin-independent early endocytic vehicles. J Cell Biol 2005;168:465–476.
102. Kirkham M, Parton RG. Clathrin-independent endocytosis: New insights into caveolae and non-caveolar lipid raft carriers. Bba-Mol Cell Res 2005;1745:273–286.
103. Sabharanjak S, Sharma P, Parton RG, Mayor S. GPI-anchored proteins are delivered to recycling endosomes via a distinct cdc42-regulated, clathrin-independent pinocytic pathway. Dev Cell 2002;2:411–423.
104. Vrljic M, Nishimura SY, Moerner WE, McConnell HM. Cholesterol depletion suppresses the translational diffusion of class II major histocompatibility complex proteins in the plasma membrane. Biophys J 2005;88:334–347.
105. Nishimura SY, Vrljic M, Klein LO, McConnell HM, Moerner WE. Cholesterol depletion induces solid-like regions in the plasma membrane. Biophys J 2006;90:927–938.
106. Shvartsman DE, Gutman O, Tietz A, Henis YI. Cyclodextrins but not compactin inhibit the lateral diffusion of membrane proteins independent of cholesterol. Traffic 2006;7:917–926.
107. Wang TY, Silvius JR. Sphingolipid partitioning into ordered domains in cholesterol-free and cholesterol-containing lipid bilayers. Biophys J 2003;84:367–378.
108. Palestini P, Allietta M, Sonnino S, Tettamanti G, Thompson TE, Tillack TW. Gel phase preference of ganglioside Gm1 at low concentration in 2-component, 2-phase phosphatidylcholine bilayers depends upon the ceramide moiety. Bba-Rev Biomembranes 1995;1235:221–230.
109. Dietrich C, Yang B, Fujiwara T, Kusumi A, Jacobson K. Relationship of lipid rafts to transient confinement zones detected by single particle tracking. Biophys J 2002;82:274–284.
110. Fisher HW, Cooper TW. Electron microscope studies of microvilli of Hela cells. J Cell Biol 1967;34:569–576.
111. Tsay JM, Doose S, Pinaud F, Weiss S. Enhancing the photoluminescence of peptide-coated nanocrystals with shell composition and UV irradiation. J Phys Chem B 2005;109:1669–1674.
112. Doose S, Tsay JM, Pinaud F, Weiss S. Comparison of photophysical and colloidal properties of biocompatible semiconductor nanocrystals using fluorescence correlation spectroscopy. Anal Chem 2005;77:2235–2242.
113. Hardman R. A toxicologic review of quantum dots: toxicity depends on physicochemical and environmental factors. Environ Health Perspect 2006;114:165–172.
114. Wilson KM, Morrison IEG, Smith PR, Fernandez N, Cherry RJ. Single particle tracking of cell-surface HLA-DR molecules using R-phycoerythrin labeled monoclonal antibodies and fluorescence digital imaging. J Cell Sci 1996;109:2101–2109.
115. Knuth KH. 2006; http://arxiv.org/abs/physics/0605197. (Unpublished).
116. Efron B, Tibshirani RJ. An Introduction to the Bootstrap. Boca Raton, FL: CRC Press; 1994.